Applied Energy 383 (2025) 125275

Contents lists available at ScienceDirect

Applied Energy

journal homepage: www.elsevier.com/locate/apenergy

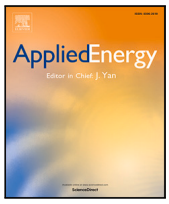

Modeling of powder bed dynamics in thermochemical heat storage

Torben Prill *, Arnulf Latz, Thomas Jahnke

Deutsches Zentrum für Luft- und Raumfahrt, Pfaffenwaldring 38-40, 70569 Stuttgart, Germany

ARTICLE INFO

Keywords:
Thermal heat storage
Powder plasticity
Simulation
Modeling

ABSTRACT

Thermochemical energy storage in the $CaO/Ca(OH)_2$ system offers high energy capacity and near perfect reversibility and is one of the most promising technologies for thermal energy storage. In particular, fixed bed reactors are being investigated for their low cost and simplicity. However, upscaling of these reactors is hindered by changes in heat and mass transfer through the powder bed due to compaction and agglomeration of the powder bed during repeated cycling. Therefore, we develop a model for the dynamics of powder beds in thermochemical reactors in response to gas flow and expansion and contraction during repeated cycling. The model couples a model for the reactive transport in the powder bed to a large strain elasto-plastic model for its deformation and compaction. The constitutive relations for the powder bed are based on modified Drucker–Prager-Cap plasticity, including a hardening mechanism. For comparison with experiment, a parametrization of the model using only flow tester data is presented. The capabilities of the new model are demonstrated by simulating multiple charge/discharge cycles, where the numerical results show irreversible effects that cannot be simulated with static models, such as successive powder compaction during cycling. The numerical results are compared with experimental data where qualitative agreement is found. Furthermore, the new model is compared with existing static models and the differences between the models are discussed. Finally, we give an outlook on how the prediction of powder compaction can lead to the design of optimized reactor geometries and cycling protocols.

1. Introduction

As countries around the world respond to climate change by moving towards renewable energy sources, being able to store large amounts of energy to offset the unpredictability of renewable energy sources and, more generally, to improve the efficiency of energy use, is becoming a key technology. Among the various means of storage, thermal energy storage can play an important role in storing thermal energy generated from renewable sources, e.g. in concentrated solar power plants, storage reactor designs for which were studied in [1,2]. Also improving the efficiency of industrial processes by storing and reusing waste heat energy offers great potential, as shown in [3].

1.1. Thermochemical energy storage

Thermochemical energy storage (TCES), where heat energy is stored in a reversible chemical reaction or sorption process, is a promising technology for large scale and long-term thermal energy storage. Among suitable materials for high temperature regimes, metal hydroxides such as $Mg(OH)_2$ or $Ca(OH)_2$, have been extensively studied due to their high energy storage density whilst being almost free of losses. Other factors favoring these materials are the fact that the storage materials are available in large quantities and that they are mostly environmentally friendly. In this paper, we investigate the $CaO/Ca(OH)_2$-system with the reversible hydration/dehydration reaction

$$CaO + H_2O \rightleftharpoons Ca(OH)_2 + \Delta H \tag{1}$$

for thermal energy storage, which is a prominent reaction system due to its high reaction enthalpy of $\Delta H = 112\,\mathrm{kJ/mol}$. An overview of the material properties of the system can be found in [4].

Energy storage in the $CaO/Ca(OH)_2$-system has been realized mainly in three reactor types: the rotary kiln reactor, the fluidized bed reactor and the fixed bed rector, the latter of which will be used as a test system for the model developed in the study. The fixed bed reactor type is widely used in research and industrial applications, and represents the earliest and simplest reactor type.

However, there are still major challenges to the up-scaling TCES fixed bed reactors, such as their relatively poor heat and mass transfer performance. As calculated by Kuipers et al. [5] and later by Schaube et al. [6], the thermal conductivity depends on the local density of the powder bed, and thus on its state of compaction. Furthermore, a

* Corresponding author.
E-mail address: torben.prill@dlr.de (T. Prill).

https://doi.org/10.1016/j.apenergy.2025.125275
Received 26 May 2024; Received in revised form 23 December 2024; Accepted 3 January 2025
Available online 20 January 2025

Nomenclature

Greek symbols

α_{min}	Minimum compression
β	β parameter of the DPC model
ΔH	Enthalpy of the thermochemical reaction
η	Lode Angle
λ	Plastic multiplier
λ_{eff}	Effective thermal conductivity of the powder bed
μ	Viscosity of the gas phase
μ_S	Shear Modulus of the powder bed
ν	Reaction rate
Φ	Plastic yield function
ϕ_α	Volume fraction of phase α
Ψ	Plastic potential
ρ_α^m	Mass density of phase α
ρ_α	Molar density of phase α
ρ_α^0	Molar density of phase α in the initial state
σ	Terzhagi's effective stress
σ_G	Physical stress in the gas phase
σ_S	Physical stress in the solid phase
θ	Angle of internal friction
ε	Linearized strain tensor
ε^l	Logarithmic strain tensor
ε_d^l	Logarithmic deviatoric strain
ε_{vol}^l	Logarithmic volumetric strain
φ	Deformation
ξ_P	Macroscopic expansion coefficient
ξ_V	Microscopic expansion factor

Operators

$\frac{D(\cdot)}{Dt}$	Material time derivative of $(\cdot)$
$\nabla(\cdot)$	Spatial gradient of $(\cdot)$
$\nabla \cdot (\cdot)$	Spatial divergence of $(\cdot)$
$\nabla_0(\cdot)$	Material gradient of $(\cdot)$
$\mathbb{1}_{dev}(\cdot)$	Deviatoric part of $(\cdot)$
$a \cdot b$	Contraction of a and b
$A : B$	Double contraction of A and B
A^T	Transpose of A
A^{-1}	Inverse of A
A^{-T}	Transpose of the inverse of A

Roman symbols

B	Cauchy strain tensor
c	Cohesion
$C_{p,\alpha}$	Heat capacity at constant pressure of phase α
d	Consolidation
d_p	Effective powder particle diameter
D_{eff}	Water vapor diffusivity
F	Total deformation gradient
F_e, F_p, F_c	Elastic, plastic, chemical deformation gradient
g	Free-fall acceleration
J	Deformation Jacobian
J^P, α	Hardening parameter of the DPC model
K_c	Cohesion parameter of the hardening model
k_h, k_d	Reaction rate constants
K_P	Yield pressure parameter of the hardening model
K_S	Young's Modulus of the powder bed
k_{bed}	Permeability of the powder bed
M_α	Molar mass of phase α
N_P^β	Plastic flow along yield surface β
p	Hydrostatic stress in the powder
p_a	Characteristic pressure of the DPC model
p_c	Critical yield pressure of the DPC model
p_G	Gas pressure in the pore-space
p_t	Critical tensile yield pressure of the DPC model
p_V	Partial vapor pressure
q	Von Mieses effective stress
R	Universal gas constant
R_P	R parameter of the DPC model
s	Deviatoric stress in the powder
T	Temperature
u_S	Solid displacement
V_α^m	Molar volume of phase α
v_S	Solid velocity
X	Material coordinate
x	Spacial coordinate
x_S	State of charge
x_V	Vapor molar fraction

significant part of the heat transfer limitation is due to a large heat transfer resistance from the reactor wall to the bed, which depends on the contact pressure between the bed and the reactor wall. Even complete detachment from the reactor wall has been observed for the SrBr-System in [7], increasing the heat flow resistance even further.

The poor heat and mass transfer, is further exacerbated by structural changes in the powder bed during cycling. This is particularly true for the reaction system which is investigated in this paper, where the powder particles agglomerate during cycling, transforming a fixed powder bed into a solid that eventually cracks during cycling. These changes also have a profound influence on the heat and mass transport through the powder bed, as has been found by Dai et al. in [8] and which has been confirmed in by parameter fitting of the permeability and conductivities of the powder bed during cycling in [9].

These structural changes in the powder bed are caused by mechanical, physical and chemical influences on the powder bed, mainly by three mechanisms. First, the gas flow through the reactor exerts a force on the powder particles, compressing the powder bed. The resulting densification of the bed increases its flow resistance while improving the heat transfer. Second, the agglomeration of powder particles, where bonds form between the particles, turning the bed into a solid. The exact mechanism of the agglomeration, however, is unknown. A theory based on particle sintering is proposed by Dai et al. in [8,10], while Afflerbach et al. [11], propose a mechanism based on particle breakage, increasing the cohesion of the powder. Thirdly, the expansion of the powder particles due to water uptake during the hydration stage, and the corresponding contraction during dehydration, causing deformation and stresses in the powder bed.

A systematic study of the changing transport properties has been done in [12], where the evolution of the porosity, permeability and the powder bed height was observed over 10 cycles. It was shown

that after the initial compaction from the pressurization, the bed compacts slightly each cycle until it reaches a maximum compaction. This is in contrast to the microscopic expansion of the powder particles, which gain up to 50% in volume. Thus, the microscopic expansion/contraction becomes increasingly decoupled from the macroscopic deformation during cycling. Also, the permeability changes between the oxide and hydroxide phases by up to two orders of magnitude, due to the changing porosity.

Therefore, a mechanical model of the local compaction, a compaction dependent thermal resistance, as well as the structural changes of the powder bed over time is needed for the computational exploration of new pathways for up-scaling of fixed bed reactors for thermochemical heat storage.

1.2. Modeling and simulation of TCES reactors

Modeling efforts for thermochemical heat storage systems have been undertaken on many different levels, a review of which can be found in [13]. The kinetics of the thermochemical reaction have been modeled for pressed pellets in [14,15], while kinetics of powder samples have been studied, among others, in [16]. An anisotropic nucleation and growth model was studied in [17] and the impact of atmospheric conditions on the kinetics was studied, e.g. in [18]. The reaction has been studied down to the molecular level in [19].

A general thermodynamically consistent model on the reactor scale has been proposed by Nagel et al. in [20] and implemented in [21–23]. An empirical model has been fitted to TCA data has been implemented by Schaube et al. in [24,25]. Further numerical modeling of fixed bed reactors has been carried out among others by Wang et al. [23,26] and Risthaus et al. [27] for cylindrical reactors, and for a rectangular reaction bed in Ranja et al. [28] . Furthermore, numerous studies focus on the optimization of the reactor design. For cylindrical reactors, Ye et al. investigated strategies to enhance the heat transfer in [29]. A multi layered reactor has been studied Han et al. [30]. Also, extensive modeling efforts have been made by Wang et al. on shell-tube reactor designs, e.g. in [31,32].

The majority of studies have assumed a constant porosity, which is not compatible with the change in volume of the powder particles during the cycling process. The modeling of permeability changes due to particle expansion in the fixed bed during cycling of thermal storage systems was first investigated by Michel et al. in [33], the simulation of these effects was first performed by Seitz in [34] for a one dimensional model and later extended to two dimensions by Xu et al. in [35].

1.3. Novelty and objective of the current study

Modeling the deformation and structural changes of the powder bed that lead to an alteration and degradation of the heat and mass transfer during cycling remains a challenge, and has not been done. The objective of this study is to address this challenge. Therefore, starting from porous media theory and taking into account assumptions specific to TECS fixed bed reactors, a model for a thermochemically active powder bed undergoing large deformation is derived. The proposed modeling allows for the simulation of new effects, such as the compaction of the powder bed due to the pressures exerted on it by the gas flow, the expansion/shrinkage of the bed during cycling, as well as irreversible effects, such as further compaction of the bed during cycling.

1.4. Outline of the paper

In the following section, we introduce the reactive transport model for the heat and mass transport inside the powder bed, by extending existing models to a dynamic powder bed on a deforming grid. Then, in Section 2.4, we present the elasto-plastic mechanical model, which defines the grid deformation based on the gas pressure and chemical expansion/shrinkage acting on the powder inside the reactor. A parametrization of the elasto-plastic constitutive model using data from Flow-Tester experiments is presented in Section 2.5. In Section 2.6 we detail the solution procedure of the model and its implementation in FEM-Software and, finally, in Section 3 we investigate the resulting behavior of the dynamic powder bed during the pressurization, charging, discharging and repeated cycling of the TCES reactor.

2. Theory

The physical model for the powder bed inside the reactor consists of two parts, a reactive transport model for the heat and mass transfer as well as the chemical reaction inside the powder bed, and a elasto-plastic mechanical model for the porous powder phase. Although the model presented in this paper is demonstrated for a moving powder bed inside a cylindrical reactor, as shown in Fig. 1, the derived equations are valid for all fixed powder bed reactors. The framework for the modeling is macroscopic porous media theory, where we consider the powder bed as a continuum composed of two phases, the solid phase S and the gas phase G. The solid phase is given by the powder particles composed of CaO and $Ca(OH)_2$, while the gas phase is the pore space in between the particles saturated with a gas mixture of nitrogen and water vapor.

In specializing the general porous media theory for TCES, the following assumptions and simplifications are made:

1. The powder bed is a porous medium composed of a solid and a fluid phase.
2. The porous medium undergoes finite elasto-plastic deformation, from the stresses resulting from the gas flow.
3. As for most powders, elastic deformations are small.
4. Powder particles do not deform due to the hydrostatic gas pressure in the pore space (see Terzhagi's effective stress).
5. The powder particles' expansion and contraction due to the chemical reaction is independent from the expansion/contraction of the macroscopic powder bed.
6. The gas flow in the pore space follows Darcy's law.
7. The molar density of the solid phase does not change from the gas-solid reaction.
8. The solid and the gas phases are in local thermal equilibrium.
9. The fluid and the solid phases are in perfect thermal and mechanical contact with the reactor walls.

Further minor assumptions as well as motivations and the choice of parameters are given in the corresponding parts of the text.

2.1. Computational domain

Due to the deformation of the powder bed we consider a domain $\Omega(t)$, which evolves over time from a initially undeformed configuration $\Omega_0 = \Omega(t = 0)$ (see Fig. 1).

The coordinates of the deformed domain $x(t) \in \Omega(t)$ are give by a deformation function φ

$$\mathbf{x}(t) = \varphi(X, t), \tag{2}$$

of the coordinates in the undeformed configuration $X \in \Omega_0$. Using the deformation φ, the deformation gradient is defined as

$$F = \frac{\partial \varphi(X, t)}{\partial X}$$

and the Jacobian J as

$$J = \det(F).$$

Further, we define the displacement u as

$$\mathbf{u}_S(t) = X - \mathbf{x}(t), \tag{3}$$

as well as its temporal derivative, denoted $\mathbf{v}_s$, as the domain deforms with the solid (powder) phase, as

$$\mathbf{v}_S(t) = \frac{\partial \varphi(X, t)}{\partial t}. \tag{4}$$

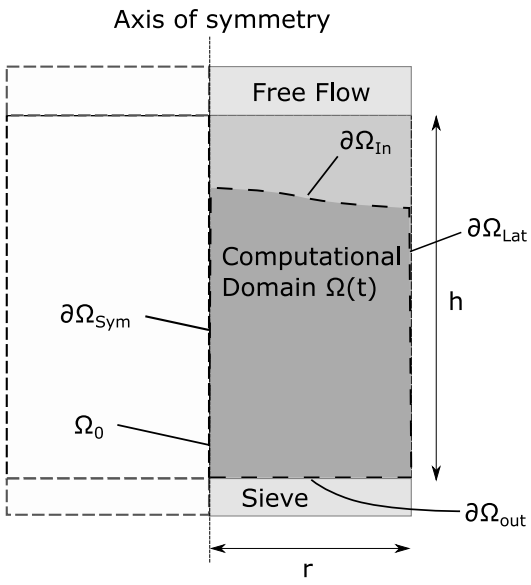

Fig. 1. Schematic of the model geometry representing a cylindrical fixed bed reactor in cylindrical coordinates (r, z). The computational domain is the powder bed $\Omega(t)$ in dark gray, bounded by the freely moving phase boundary at the top $\partial\Omega_{in}$ and the fixed outflow at the bottom. At the left boundary $\partial\Omega_{sym}$ symmetry boundary conditions apply, while at the right the domain is bounded by the fixed reactor wall $\partial\Omega_{lat}$.

The velocity v_S and the Jacobian J are connected by the identity

$$\frac{\partial J(t)}{\partial t} = J(t)\nabla \cdot v_S. \tag{5}$$

Moreover, the material time derivative of a scalar function f, transported with the velocity $\mathbf{v}_S$ is defined as

$$\frac{Df}{Dt} = \frac{\partial f}{\partial t} + \nabla f \cdot \mathbf{v}_S, \tag{6}$$

where derivatives without subscript are taken with respect to spacial coordinates x. The material time derivative defines the temporal derivative of a function transported on the moving domain $\Omega(t)$. As the model is solved on a grid deforming with $\Omega(t)$, the reactive transport model is formulated in terms of the material time derivatives.

Using $\mathbf{u}_S$, the deformation gradient can be expressed as:

$$F = \mathbb{1} + \nabla_0 \mathbf{u}_S \tag{7}$$

with the identity tensor $\mathbb{1}$ and the derivative in material coordinates ∇_0, where the suffix "0" indicates a derivatives taken with respect to the undeformed configuration, i.e. with respect to material coordinates X.

Using these quantities, we define the Cauchy strain tensor as

$$B = FF^T, \tag{8}$$

and the logarithmic (spatial) strain tensor

$$\varepsilon^l = \frac{1}{2}\log B. \tag{9}$$

Accordingly, the volumetric and deviatoric strains are defined as

$$\begin{aligned} \varepsilon^l_{vol} &= \mathrm{tr}(\varepsilon^l), \\ \varepsilon^l_d &= \mathbb{1}_{dev}(\varepsilon^l) = \varepsilon^l - \frac{1}{3}\mathrm{tr}(\varepsilon^l)\mathbb{1}, \end{aligned} \tag{10}$$

with the identity tensor $\mathbb{1}$ and the deviatoric part of the strain tensor with $\mathbb{1}_{dev}(\cdot) = (\cdot) - \frac{1}{3}\mathrm{tr}(\cdot)\mathbb{1}$. Using (10), the Jacobian can be written as

$$J = e^{\varepsilon^l_{vol}}. \tag{11}$$

2.2. Reactive transport

The reactive transport model is adapted from [20], with the added assumption of local thermal equilibrium as in [23] and a varying porosity of the powder bed as in [34]. As mentioned above, the model considers a macroscopic porous medium consisting of two phases, the solid phase S and the gas phase G. The respective volume fractions for the gas and solid phases are ϕ_S and ϕ_G are

$$\phi_\alpha(t) = \frac{\left|\hat{\Omega}_\alpha(t)\right|}{\left|\hat{\Omega}(t)\right|}, \tag{12}$$

where $\hat{\Omega}(t)$ is an arbitrary subvolume of $\Omega(t) \supseteq \hat{\Omega}(t)$ and $\hat{\Omega}_\alpha(t) \subseteq \hat{\Omega}(t)$ is the subvolume occupied by phase α in the current configuration. As the porous medium deforms, the saturation condition becomes

$$\phi_G(t) + \phi_S(t) = 1, \tag{13}$$

with the current volume fractions $\phi_S(t)$ and $\phi_G(t)$.

The reactive transport model is written in terms of the primary variables p_G, T, x_V, x_S, which are the pressure of the gas phase in the pore space, the local temperature (averaged over all phases), the molar fraction of water vapor in the gas phase and the molar fraction of CaO in the solid phase.

2.2.1. Solid phase molar balance

The molar balances of the components $\alpha \in \{\mathrm{CaO}, \mathrm{Ca(OH)_2}\}$ of the solid phase are given in local form by

$$\frac{\partial \rho_\alpha}{\partial t} + \nabla \cdot (\rho_\alpha \mathbf{v}_S) = \beta\hat{\rho}, \tag{14}$$

where ρ_α is the molar density of the phase α, $\hat{\rho}$ is a source/sink term from the thermochemical reaction given in 2.3, and $\beta \in \{-1, 1\}$ is a factor indicating whether the phase gains or loses species amount when the solid absorbs water. I.e. $\beta = 1$ for $\mathrm{Ca(OH)_2}$ and $\beta = -1$ for CaO.

Using the material time derivative, (14) can be rewritten as

$$\frac{D\rho_\alpha}{Dt} + \rho_\alpha \nabla \cdot \mathbf{v}_S = \beta\hat{\rho}. \tag{15}$$

Adding the component molar balances gives the total molar balance of the solid phases

$$\frac{D\rho_S}{Dt} + \rho_S \nabla \cdot \mathbf{v}_S = 0, \tag{16}$$

where $\rho_S = \rho_{\mathrm{CaO}} + \rho_{\mathrm{Ca(OH)_2}}$ is the total solid molar density. Using (11), (16) has the analytical solution

$$\rho_S(t) = \rho_S^0 \exp\left(-tr(\varepsilon^l)\right) = \rho_S^0 J^{-1}, \tag{17}$$

where ρ_S^0 is the initial molar concentration in the powder bed, given by $\rho_S^0 = \phi_S^0 \rho_{S,R}$, where $\rho_{S,R}$ is the physical/tabulated molar density of the storage material (in this model $\mathrm{Ca(OH)_2}$).

CaO component molar balance. As the overall molar density of the solid phase is conserved, the density of oxide ρ_{CaO} can be written as the molar fraction of CaO in the solid phase

$$\rho_{\mathrm{CaO}} = x_S \rho_S \tag{18}$$

where

$$x_S = \frac{\rho_{\mathrm{CaO}}}{\rho_{\mathrm{CaO}} + \rho_{\mathrm{Ca(OH)_2}}} \in [0, 1]$$

is the state of charge (SOC), a dimensionless number indicating the reaction progress, where $x_s = 1$ corresponds to pure CaO and $x_s = 0$ corresponds to pure $\mathrm{Ca(OH)_2}$, respectively. Then, the CaO molar balance can be rewritten as

$$\frac{D(x_S\rho_S)}{Dt} + x_S\rho_S \nabla \cdot \mathbf{v}_S = -\hat{\rho} \tag{19}$$

which, again using (16) can be rewritten as

$$\rho_S \frac{Dx_S}{Dt} = -\hat{\rho}. \tag{20}$$

Porosity. The solid volume fraction (SVF), which is needed to calculate the porosity in the following, is given by the SVFs of the components of the solid phase

$$\phi_S = \sum_\alpha \phi_\alpha = \sum_\alpha \rho_\alpha V_\alpha^m, \tag{21}$$

where ρ_α is the density of the solid phase. In terms of molar fractions, this gives

$$\phi_S = \rho_S \left(x_S V_{\mathrm{CaO}}^m + (1 - x_S) V_{\mathrm{Ca(OH)_2}}^m \right) \tag{22}$$

with the molar volumes of the constituent phases of the solid phase V_α^m. Using (17) this can be reformulated as

$$\phi_S(t, x_S) = \rho_S^0 J^{-1} V_{\mathrm{Ca(OH)_2}}^m \left(1 - x_S \xi_V\right), \tag{23}$$

in terms of the initial density ρ_0^S and an expansion factor

$$\xi_V = 1 - \frac{V_{\mathrm{CaO}}^m}{V_{\mathrm{Ca(OH)_2}}^m} \approx 0.502. \tag{24}$$

Using the saturation condition (13) yields the porosity

$$\phi_G(t) = 1 - \phi_S(t, x_S). \tag{25}$$

2.2.2. Gas phase mass balance

The molar balance of the gas phase inside the porous powder bed is given by

$$\frac{\partial(\phi_G \rho_G)}{\partial t} + \nabla \cdot (\phi_G \rho_G \mathbf{v}_G) = \hat{\rho}, \tag{26}$$

where ϕ_G is the volume fraction of the pore space, given by (13) and, and ρ_G is the physical density of the gas inside the pore space. Also, as only water vapor is exchanged between the phases, only one source term is $\hat{\rho}$ for all balance equations is needed. Again, using the material time derivative, Eq. (26) can be written as

$$\begin{aligned} &\frac{\partial(\phi_G \rho_G)}{\partial t} + \nabla \cdot \left(\phi_G \rho_G (\mathbf{v}_f + \mathbf{v}_S)\right) = \hat{\rho} \\ &\frac{D(\phi_G \rho_G)}{Dt} + (\phi_G \rho_G) \nabla \cdot \mathbf{v}_S + \nabla \cdot (\phi_G \rho_G \mathbf{v}_f) = \hat{\rho}, \end{aligned} \tag{27}$$

where the velocity $\mathbf{v}_f$ denotes the filtration velocity, given by $\mathbf{v}_f = \mathbf{v}_G - \mathbf{v}_S$, i.e. the relative velocity of the gas phase flowing through the powder bed. Expanding the temporal derivative and using the fact that

$$\begin{aligned} \frac{D\phi_G}{Dt} &= \frac{\partial \phi_G}{\partial x_S} \frac{Dx_S}{Dt} + \frac{\partial \phi_G}{\partial \rho_S} \frac{D\rho_S}{Dt} \\ &= V_{\mathrm{Ca(OH)_2}}^m \hat{\rho} + (1 - \phi_G) \nabla \cdot v_S, \end{aligned} \tag{28}$$

(27) can be further simplified to:

$$\begin{aligned} \phi_G \frac{D\rho_G}{Dt} + \rho_G \nabla \cdot \mathbf{v}_S + \nabla \cdot (\phi_G \rho_G \mathbf{v}_f) \\ = \hat{\rho}(1 - \rho_G V_{\mathrm{Ca(OH)_2}}^m \xi_V). \end{aligned} \tag{29}$$

Using the ideal gas law

$$\frac{p_G}{\rho_G} = RT \tag{30}$$

this molar balance equation can be rewritten in terms of the primary variables to give

$$\begin{aligned} \frac{\phi_G}{TR} \frac{Dp_G}{Dt} - \phi_G \frac{\rho_G}{T} \frac{DT}{Dt} + \rho_G \nabla \cdot \mathbf{v}_S + \nabla \cdot (\phi_G \rho_G \mathbf{v}_f) \\ = \hat{\rho}(1 - \rho_G V_{\mathrm{Ca(OH)_2}}^m \xi_V). \end{aligned} \tag{31}$$

where R is the universal gas constant and $\hat{\rho}$ is a source/sink term due to the thermochemical reaction (see [20] for details).

The filtration velocity v_f is expressed in terms if the Darcy velocity of the gas phase inside the powder bed, given by

$$\mathbf{v}_f = \frac{v_D}{\phi_G} = \frac{k_{pm}(\phi_G)}{\phi_G \mu} \nabla p_G \tag{32}$$

where the dynamic viscosity was implemented from the fourth order approximation in the VDI-Wärmeatlas [36]. A Kozeny-Karman type relation was assumed for the porosity dependence of the permeability of the powder bed:

$$k_{bed}(\phi) = d_p^2 \frac{\phi_G^3}{180(1 - \phi_G)^2}, \tag{33}$$

where d_p is an effective powder particle diameter of the bed.

2.2.3. Vapor component molar balance

The molar balance for the water vapor is written in terms of a dimensionless molar fraction of gaseous water in nitrogen x_v and is given by

$$\frac{\partial(\phi_G x_V \rho_G)}{\partial t} + \nabla \cdot (\phi_G x_V \rho_G \mathbf{v}_G) = \hat{\rho}, \tag{34}$$

Using the approximations for the diffusion term in [20] and the material time derivative, gives:

$$\begin{aligned} \phi_G \rho_G \frac{Dx_V}{Dt} - \nabla \cdot (\rho_G D_{\mathrm{eff}} \nabla x_V) + \phi_G \rho_G \nabla x_V \cdot \mathbf{v}_f \\ - \hat{\rho}(1 - x_V) = 0, \end{aligned} \tag{35}$$

with the effective diffusion coefficient D_{eff} of gaseous water in nitrogen, inside the pore space of the powder bed.

2.2.4. Energy balance

Following [23], we assume local thermal equilibrium and write the energy balance in terms of the gas phase enthalpy as

$$\begin{aligned} \rho_S [C_P]_{Mix} \frac{\partial T}{\partial t} - \frac{\partial(\phi_G p_G)}{\partial t} - \nabla \cdot (\lambda_{\mathrm{eff}} \nabla T) \\ + \rho_G C_{p,G} \nabla T \cdot \mathbf{v}_G = -\hat{\rho} \Delta H \end{aligned} \tag{36}$$

with the thermal conductivity λ_{eff} of the powder bed and the specific molar heat capacity of the gas phase $C_{P,G}$ (the heat capacity of the gas phase is neglected in the storage term). The specific heat capacity of the solid mixture is given by the weighted average:

$$\begin{aligned} [C_P]_{Mix} &= \left[C_{P,\mathrm{CaO}} \rho_{\mathrm{CaO}} + C_{P,\mathrm{Ca(OH)_2}} \rho_{\mathrm{Ca(OH)_2}} \right] \\ &= \left[M_{\mathrm{CaO}} C_{P,\mathrm{CaO}} x_S + M_{\mathrm{Ca(OH)_2}} C_{P,\mathrm{Ca(OH)_2}} (1 - x_S) \right]. \end{aligned} \tag{37}$$

An analogous expression is used for the specific heat capacity of the gas phase.

Using the material time derivative, the energy equation on the deforming grid becomes:

$$\begin{aligned} \rho_S [C_P]_{Mix} \frac{DT}{Dt} - \frac{D(\phi_G p_G)}{Dt} - \nabla \cdot (\lambda_{\mathrm{eff}} \nabla T) \\ + \rho_G C_{p,G} \nabla T \cdot \mathbf{v}_f = -\hat{\rho} \Delta H. \end{aligned} \tag{38}$$

Finally, the enthalpy production from the thermochemical reaction (1) is $\Delta H = 112$ kJ/mol.

2.3. Reaction

The reaction rate ν for the thermochemical reaction (1) is given by the first order reaction kinetics:

$$\nu = \begin{cases} k_h x_V x_S \frac{T_{eq}(p_V) - T}{T_{eq}(p_V)} & , T_{eq}(p_V) - T \geq 0 \\ k_d (1 - x_S) \frac{T_{eq}(p_V) - T}{T_{eq}(p_V)} & , T_{eq}(p_V) - T < 0 \end{cases} \tag{39}$$

depending on the rate constants k_h, k_d, the mass fractions in the gaseous and solid reactants, and the distance of the local temperature T from the thermodynamic equilibrium temperature $T_{eq}(p_V)$. A fit from Schaube et al. [16] is used for the equilibrium temperature:

$$T_{eq}(p_V) = \frac{-12845}{\log(p_V / 10^5) - 16.508}. \tag{40}$$

The equilibrium temperature, in turn, depends on the partial pressure of water vapor in the gas phase, which can be calculated from the gas pressure p_G and the molar water fraction x_V:

$$p_V = p_G x_V. \tag{41}$$

Using the reaction rate (39), the source term in the mass balance equations is given by:

$$\hat{\rho} = \rho_S \nu. \tag{42}$$

2.4. Elasto-plastic model

The reactive transport model is coupled to a mechanical model for the deformation of the powder bed itself. Primary variables of the model are the three components of the solid phase displacement $\mathbf{u}_S(X,t)$ from the undeformed configuration and the plastic strain ε_p. The coupling of the mechanical model to the reactive transport model occurs through the expansion/contraction of the powder bed due to the chemical reaction, as well as the force exerted on the powder by the gas flow. While the momentum transfer from the solid to the gas is neglected, a backward coupling exists through the dependence of the porosity ϕ_G on the displacement in (25).

Momentum balance. To compute the momentum balance in the solid phase, the volume average stress in the porous medium is given by

$$\langle\sigma\rangle = \phi_S\sigma_S + \phi_G\sigma_G, \tag{43}$$

where σ_S and σ_G are the stresses in the solid and gas phases, respectively. Assuming Darcy-flow in the pore-space, the stress in the gas phase is purely hydrostatic, given by $\sigma_G = p_G\mathbb{1}$. Using this, Terzhagi's effective stress in the solid phase σ is defined as

$$\sigma = \phi_S(\sigma_S - p_G\mathbb{1}), \tag{44}$$

which is the mechanical load per unit area supported by the solid phase. As this stress measure corresponds to the average stresses in the material in a drained condition under mechanical load, it can be used directly for the parametrization with mechanical experiments (see 2.5).

Including gravity, the momentum balance in the solid phase is then given by

$$0 = \nabla\cdot\sigma + \mathbf{f}, \tag{45}$$

with the effective Cauchy stress tensor σ in the solid phase and the driving force $\mathbf{f}$, given by the gradient of the gas pressure and gravity

$$\mathbf{f} = -\nabla\cdot p_G + g\rho_S^m. \tag{46}$$

The mass density ρ_S^m is expressed with the molar masses of the solid phases

$$\rho_S^m = \rho_S(M_{\mathrm{CaO}}x_S + M_{\mathrm{Ca(OH)_2}}(1-x_S)). \tag{47}$$

2.4.1. Constitutive model

A multiplicative splitting of the deformation gradient is assumed for the elasto-plastic constitutive model, including the shrinkage and swelling of the powder during the reaction, i.e.

$$F = F_eF_pF_c \tag{48}$$

where F_e is the deformation gradient leading to elastic stresses and F_p and F_c are the plastic and chemical deformation gradients leading to stress-free intermediate configurations via plastic deformation and swelling/shrinkage.

Expansion/contraction. During the hydration the bed absorbs water, increasing the volume of the individual particles. However, as was shown in [12], the microscopic expansion leads to only a small increase in the macroscopic volume of the powder bed. Therefore, the microscopic and the macroscopic expansion and contraction are decoupled in the model, where the microscopic expansion enters the solid volume fraction (22) via the factor ξ_V, the macroscopic expansion is modeled by the chemical strain, which is given by an isotropic contraction or expansion

$$F_c = (1 + x_S\xi_P)\mathbb{1} \tag{49}$$

with the identity tensor $\mathbb{1}$ and the volumetric expansion coefficient ξ_P, given by

$$\xi_P = \frac{\Delta V}{V}. \tag{50}$$

In general, the volumetric expansion coefficient ξ_P is different from ξ_V in (24). While ξ_V is the expansion of the volume of the solid phase in the porous medium, ξ_P is the expansion of the powder bed itself. Thus, if $\xi_V > \xi_P$, the porosity of the bed decreases during expansion as the solid phase expands into the pore space, and it increases if $\xi_V < \xi_P$. Empirically, we assume an expansion factor of $\xi_P = 0.05 < \xi_V$, so that most of the expansion of the solid phase goes into the pore space, while the rest leads to a macroscopic expansion of the powder bed.

Elastic model. The elastic stress can be calculated using the elastic strain

$$\varepsilon_{el}^l = \frac{1}{2}\log B_e \tag{51}$$

with $B_e = F_eF_e^T$. Using (48) results in

$$F_e = FF_c^{-1}F_p^{-1} \tag{52}$$

and thus

$$B_e = FF_c^{-1}F_p^{-1}F_p^{-T}F_c^{-T}F^T. \tag{53}$$

Using the fact that F_c commutes with all deformation gradients leads to the decomposition

$$B_e = FF_p^{-1}F_p^{-T}F^TB_c^{-1}. \tag{54}$$

Furthermore, we can assume that for the present powder, the elastic deformation is small compared to the plastic deformation. Therefore, $F \approx F_p$, and most importantly, F is approximately colinear with F_p. Using the argument in Miehe [37], both approximately commute and B_e approximately factorizes to

$$B_e = BB_p^{-1}B_c^{-1} \tag{55}$$

which leads to the approximate decomposition of the logarithmic strain

$$\sigma = \mathbb{C} : \varepsilon_{el}^l = \mathbb{C} : (\varepsilon^l - \varepsilon_p^l - \varepsilon_c^l), \tag{56}$$

where ε^l, ε_{el}^l, and ε_p^l are the total, elastic, and plastic strain tensors, respectively, and $\mathbb{C}$ is the fourth-order elastic stiffness tensor. The tensor ε_c^l is the chemical strain term induced by the expansion and shrinkage of the powder during de-/hydration.

A constitutive model for the elastic stresses is defined using the parameters K_S and μ_S, i.e., the bulk and shear moduli, respectively, as follows

$$\sigma = \mathbb{C} : \varepsilon_{el}^l = K_S\mathrm{tr}(\varepsilon_{el}^l)\mathbb{1} + 2\mu_S\mathbb{1}_{dev}(\varepsilon_{el}^l). \tag{57}$$

The bulk and shear moduli can be calculated from Young's modulus E_S and Poisson's ratio ν_S via

$$K_S = \frac{E_S}{3(1-2\nu_S)}, \qquad \mu_S = \frac{E_S}{2(1+\nu_S)}.$$

To be consistent with the assumption that the bed deforms mostly plastically the Young's modulus must be much larger than the pressure drop across the reactor, which is the largest pressure in the system, i.e. $E_S \gg P_{in} - P_{out}$.

Linearization. While the use of logarithmic strain allows the formulation of a consistent theory for large strain elasto-plasticity, the solution of the resulting models is computationally challenging. Therefore, the model is linearized, similar to the linearized large deformation model in [38], yielding

$$\varepsilon = \frac{1}{2}(F + F^T) = \frac{1}{2}\left(\nabla_0 u_S + (\nabla_0 u_S)^T\right). \tag{58}$$

Using that $\nabla_0(\cdot) = \nabla F(\cdot)$, the linearized Eulerian strain is given by

$$\varepsilon = \frac{1}{2}\left(\nabla F u_S + (\nabla F u_S)^T\right). \tag{59}$$

2.4.2. Plastic model

As in [39–42], we assume that the plastic yield surface follows a modified Drucker–Prager-Cap (DPC) Model, first introduced in [43]. Thus, a plastic yield surface is defined by the zero level set of a function $\Phi(\sigma)$, where the material response is elastic for $\Phi(\sigma) < 0$ and plastic flow occurs when $\Phi(\sigma) = 0$. As shown in Fig. 2, the plastic yield surface depends on the hydrostatic pressure, i.e. the yield function is given by the two functions $\Phi^C(\sigma)$ and $\Phi^{DP}(\sigma)$, which are augmented by the function $\Phi^T(\sigma)$ for tensile loads. The exact definition of these functions is in given the following paragraph.

As is standard for large strain plasticity, the evolution of the plastic deformation gradient is given in rate form by a flow rule. For large strain elastoplasticity we adopt the approach in [44]. With the flow rule given by

$$\begin{aligned} \dot{F}_p &= \dot{\lambda} N_p(\sigma, \alpha) F_p, \\ N_p(\sigma) &= \sum_i \rho_i(\sigma) \frac{\partial \Psi_i}{\partial \sigma}, \end{aligned} \tag{60}$$

which depends on the plastic potentials Ψ_i for $i \in \{C, DP, T\}$. In the case of an associated flow rule, the yield function Φ_i is identical to the plastic potential Ψ_i, in the case of a non-associated flow rule, Ψ_i is different from Φ_i. The function $\rho(\sigma)$, selects the active yield surface according to the stress state

$$\rho_i(\sigma) = \begin{cases} 1 & \Phi_i(\sigma) \geq 0 \\ 0 & \Phi_i(\sigma) < 0 \end{cases} \tag{61}$$

The parameters λ_i are determined by the consistency conditions

$$\Phi(\sigma) \leq 0, \qquad \dot{\lambda} \geq 0, \qquad \dot{\lambda}\Phi = 0. \tag{62}$$

Solving the evolution equation for a single timestep yields the incremental form

$$F_p^{n+1} = \exp\left(\delta\lambda N_p\right) F_p^n. \tag{63}$$

As shown, among others, in [45], using the multiplicative split (48) and the definition of the logarithmic elastic strain, the incremental form can be expressed as an additive update in the logarithmic strains

$$\begin{aligned} \varepsilon^l_{e,n+1} &= \varepsilon^l_{e,tr} + \delta\lambda N_p(\sigma) \\ N_p &= \sum_i \rho_i(\sigma) \frac{\partial \Psi_i}{\partial \sigma} = N_p^C + N_p^{DP} + N_p^T. \end{aligned} \tag{64}$$

for some trial strain $\varepsilon^l_{e,tr}$. Finally, for a unique determination of the plastic flow, the parameters λ_i are given by the condition

$$\Phi(\sigma + \delta\lambda N_p) = 0 \tag{65}$$

for $i \in \{C, DP, T\}$.

Yield surface and flow rule. The yield surface for the DPC model is defined in terms of the stress invariants $p(\sigma)$ and $q(\sigma)$. The yield surface is shown in p/q-space in Fig. 2 and depends on the dimensionless parameters R_P, β and the characteristic pressure p_c.

The stress invariant p is the hydrostatic stress

$$p = \frac{1}{3}\mathrm{tr}(\sigma), \tag{66}$$

while q is the von Mieses norm of the stress tensor

$$q = \sqrt{\frac{3}{2} s : s}, \tag{67}$$

where s is the deviatoric part of the stress tensor σ, is given by

$$s = \mathbb{1}_{dev}(\sigma) = \sigma - \frac{1}{3}\mathrm{tr}(\sigma). \tag{68}$$

Which yield function is active depends on the hydrostatic stress, where we distinguish between three cases, depending on the characteristic

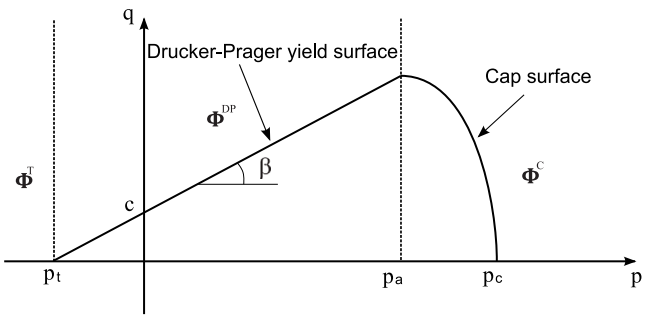

Fig. 2. A plot of the yield surface of the Drucker–Prager-Cap model. The model consists of two yield surfaces defined for different hydrostatic pressures p: the Cap surface, given by $\Phi_C = 0$ for $(p > p_a)$, the Drucker–Prager yield surface, given by $\Phi_{DP} = 0$ for $(p_a > p > p_t)$, augmented by the yield function for $\Phi_T = 0$ for tensile yield $(p < p_t)$.

pressures p_c, p_a and p_t, marked in Fig. 2 on the p-axis. The characteristic pressure p_a is given by

$$p_a = \frac{p_c - R_P c}{1 + R_P \tan(\beta)} \tag{69}$$

and depends on the critical yield pressure p_c, which is a parameter of the model and is determined by fitting to data as shown in Section 2.5. For yielding under tensile strain, we define the critical yield pressure

$$p_t = \frac{-c}{\tan(\beta)}. \tag{70}$$

For $p \geq p_a$, the plastic potential is given by the Cap-Function Φ^C depending on the pressure p_a, and the parameter R parameterizing the curvature of the yield surface

$$\Phi_C = \sqrt{(p_a - p)^2 + (R_P q)^2} - R_P\left(c + p_a \tan(\beta)\right). \tag{71}$$

Plastic flow is given by the associated flow rule

$$\begin{aligned} N_p^C &= \rho_C(\sigma) \frac{\partial \Phi_C}{\partial \sigma}, \\ &= \rho_C(\sigma) \frac{1}{\sigma_C^{eq}} \left(-\frac{1}{3}(p_a - p)\mathbb{1} + \frac{3R_P}{2} s\right), \end{aligned} \tag{72}$$

with the equivalent stress σ_C^{eq} given by

$$\sigma_C^{eq} = \sqrt{(p - p_a)^2 + (R_P q)^2}.$$

For $p_t < p < p_a$ the plastic potential is given by the well-known Drucker–Prager yield criterion, depending on the angle β and the cohesion c,

$$\Phi_{DP} = q - \tan(\beta)p - c. \tag{73}$$

In this case a non-associated flow rule with pure shear is postulated

$$N_p^{DP} = \rho_{DP}(\sigma) \frac{3s}{2q}. \tag{74}$$

resulting in volume conserving plastic flow.

For $p \leq p_t$ the plastic potential is given by

$$\Phi_T = \sqrt{(p - p_t)^2 + q^2}, \tag{75}$$

again with an associated flow-rule

$$\begin{aligned} N_p^T &= \rho_T(\sigma) \frac{\partial \Phi_T}{\partial \sigma}, \\ &= \rho_T(\sigma) \frac{1}{\sigma_T^{eq}} \left(\frac{1}{3}(p - p_t)\mathbb{1} + \frac{3}{2} s\right) \end{aligned} \tag{76}$$

again with the equivalent stress

$$\sigma_T^{eq} = \sqrt{(p - p_t)^2 + q^2}.$$

Isotropic hardening. In accordance with the modified Drucker–Prager-Cap model, consolidation is modeled as a hardening of the plastic yield surface, i.e. as a dependency of the yield pressure on the compression of the powder. To this end, the parameter α is introduced as

$$\alpha = J^P = \det(F_p) = \exp(\mathrm{tr}(\varepsilon_p^I)) \tag{77}$$

and the critical yield pressure $p_c(\alpha)$, as well as the cohesion $c(\alpha)$ are a function of α. The general form of the hardening model is adapted from [46], which introduces the minimum compression α_{min}, where the particles are maximally densely packed and the mechanical properties are dominated by the elastic compression of the powder particles themselves, which are approximated by the bulk elastic properties. The model for p_c is given by

$$p_c = -K_P \log\left(1 - \frac{1-\alpha}{\alpha_{min}}\right), \tag{78}$$

where the parameters K_P, α_{min} are subject to fitting to experimental data.

Analogously, it is assumed that the cohesion grows linearly with compression, i.e.

$$c(\alpha) = K_c(1-\alpha) + c_0, \tag{79}$$

again with the parameters K_c and c_0 fitted to data.

Linearization. Given that the incremental form of the flow rule (64) is already linear, the plastic model can be trivially linearized. However, to be consistent with the isotropic linear strain in (59), the Jacobian in (11) is linearized with the approximation

$$\alpha = J^P = \exp(\mathrm{tr}(\varepsilon_p^I)) \approx 1 + \mathrm{tr}(\varepsilon_p). \tag{80}$$

A preexisting compaction of the powder bed can be simulated by linearizing the model around the preconsolidated state. Then the hardening parameter becomes

$$\alpha = J^{pre} J^P \approx J^{pre}(1 + \mathrm{tr}(\varepsilon_p)). \tag{81}$$

The complete elasto-plastic model is given by Eqs. (45), (64), (62), i.e. the momentum balance, the flow-rule and the consistency condition. The elasto-plastic system of the model takes the form

$$\frac{d}{dt}\begin{pmatrix}\varepsilon_p\\ \alpha\\ 0\\ 0\end{pmatrix} = \begin{pmatrix}\lambda \sum_i \rho_i(\sigma)\frac{\partial \Psi_i}{\partial \sigma}\\ \lambda(\rho_T \frac{\partial \Phi_T}{\partial \alpha} + \rho_C \frac{\partial \Phi_C}{\partial \alpha})\\ \boldsymbol{\Phi}(\sigma_{el} + \lambda \mathbb{C} : N_p)\\ \nabla \cdot \mathbb{C} : (\varepsilon - \varepsilon_p - \varepsilon_c(x_s)) + \mathbf{f}(p, J)\end{pmatrix}$$

As the plastic multiplier λ and the displacements $\vec{u}_S$ do not appear with a time derivative the system constitutes a differential–algebraic system of equations (DAE). Further, the index of the system is 2 (see e.g. [47]), which carries over to the complete model system including the reactive transport.

2.5. Parametrization of the yield surfaces

Flow tester data in [48] was used to parameterize the yield surface by fitting the Drucker–Prager model to the existing data set. To this end, data from a shear cell experiment was used to parameterize a Coulomb–Mohr-Yield-Surface, which was in turn used to parameterize a Drucker–Prager-Yield-Surface, given an assumption on the value of the Lode-Angle.

2.5.1. Flow tester experiments

The data was obtained from experiments using a commercially available PSL (Powder Flow Tester PFT, Brookfield). The flow tester measures the uniaxial yield strength σ_c over an increasing uniaxial consolidation stress σ_1, which can be used to parameterize the Drucker–Prager yield surface, i.e. the angle of internal friction and cohesion. In addition, the powder density was measured over an increasing consolidation stress, which allows the parametrization of the cap portion of the yield surface by calculating the critical yield pressure as a function of compression. Since the tests cannot distinguish between elastic and plastic stresses, it is assumed that the deformation is purely plastic, which is approximately consistent with the model assumptions of small elastic strains.

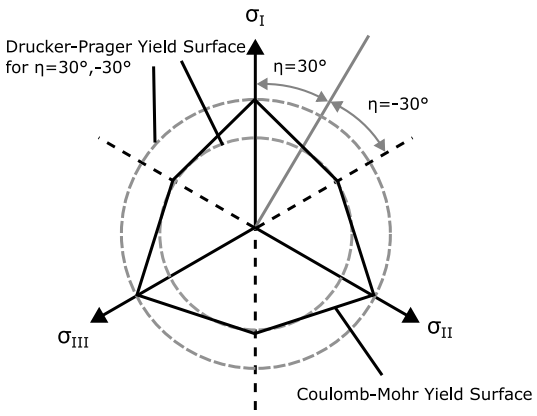

Fig. 3. The Coulomb–Mohr (solid) and Drucker–Prager (dashed) yield surfaces projected on the principal stresses σ_I-σ_{III}, for different Lode angles η.

2.5.2. Coulomb–Mohr yield surface

For the parametrization of the Drucker–Prager part of the yield surface, the flow tester measured the linear axial compressive strength (unconfined yield strength) σ_c over an increasing consolidation stress. This data can be used to compute the yield locus and consolidation d, as well as the angle of internal friction θ to parameterize a Coulomb–Mohr failure criterion

$$\tau = d + q \tan\theta \tag{82}$$

As shown in [40], this data can in turn be used to parameterize the Drucker–Prager model, given by Eq. (73). However, the transition from the Coulomb–Mohr- to Drucker–Prager model is not unique and depends on assumptions about the so-called Lode angle η. An illustration of the Lode angle is shown in Fig. 3. When projected onto the space of principal stresses $(\sigma_I, \sigma_{II}, \sigma_{III})$, the Coulomb–Mohr failure criterion is given by six faces, while the Drucker–Prager failure criterion is given by a circle. As the fit from the Coulomb–Mohr to the Drucker–Prager yield surface is not unique, it is assumed in this study, that the Druck–Prager circle in principal stress space inscribes the Coulomb–Mohr yield surface (see Fig. 3). Then, the parameters of the Drucker–Prager yield surface depend on the Coulomb–Mohr parameters by

$$\tan\beta = \frac{3\sin\theta}{\sqrt{3}\cos\eta - \sin\theta\sin\eta}, \tag{83}$$

$$c = \frac{3c\cos\theta}{\sqrt{3}\cos\eta - \sin\theta\sin\eta}. \tag{84}$$

Since the exact stress state in the flow tester is unknown, it is argued in [40] that the Lode angle cannot possibly be determined from flow tester experiments alone, hence, we shall postulate a angle of $\eta = 0°$ in this study. The first parameter of the Coulomb–Mohr yield surface is the cohesion $d(\alpha)$, which was also determined from flow tester experiments. In the model it is assumed that the equation depends linearly on the compression factor α, which yields a very good fit, as can be seen in Fig. 4.

From the data, the best fit model it obtained as

$$d(\alpha) = 1.21656(1-\alpha) - 0.0857497. \tag{85}$$

The final parameter to be determined is the internal friction angle θ. As can be seen in Fig. 5, θ does not show great dispersion around its mean value of $\theta = 29.72°$, which was taken for the model.

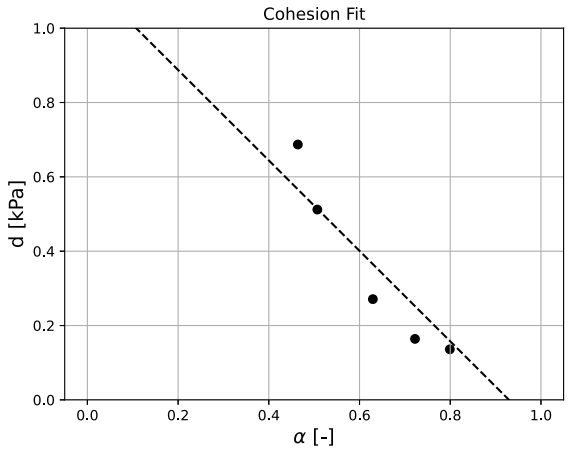

Fig. 4. Fitting of the cohesion parameter in the Coulomb–Mohr failure criterion to hardening parameter α. Dots indicate data points from flow tester experiments while the dashed line indicates the fitted linear function in Eq. (85).

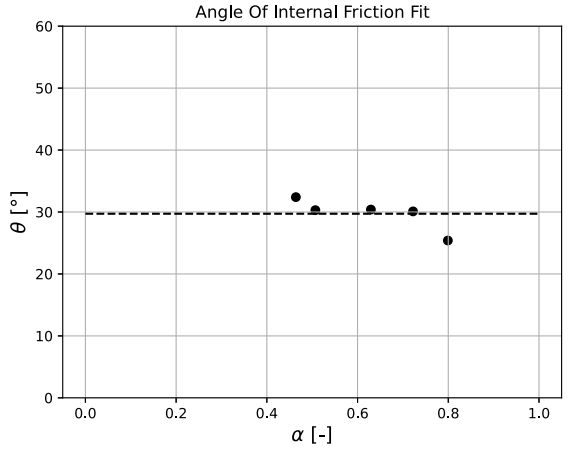

Fig. 5. Fitting of the angle of internal friction θ. Dots indicate data points from flow tester experiments, the dashed line indicates the mean angle of $\beta = 29.72°$.

2.5.3. Drucker–prager yield surface

Given the fitted parametrization of the Coulomb–Mohr yield surface, we determined the parameters for the Drucker–Prager yield surface using Eqs. (83), (84). However, as the ambiguity in the Lode angle leads to an ambiguity in the parameters $c(\phi)$ and β. The range of possible values for $\tan\beta$ and c can be determined by a variation of the Lode angle within its possible values of $\eta \in [-30°, 30°]$. As shown in Fig. 6, the possible values of β range between 39.54° and 49.9°, where the minimum is assumed at $\eta = -15.97°$ and the maximum is at the maximum Lode angle of $\eta = 30°$.

The corresponding dependence of the cohesion is shown in Fig. 7. As shown, for all values, the variation is similar to the one of β, with the cohesion varying between a minimum at $\eta = -24.62°$ and maximum at $\eta = 30°$. The overall maximum of the cohesion for the highest pressure is $c = 1.19$ kPa.

The parameters for final Drucker–Prager Yield surfaces given by Eq. (73), fitted to flow tester experiments, where a Lode angle of $\eta = 0°$ has been assumed, are

$$\tan(\beta) = 0.858685, \tag{86}$$

$$c(\alpha) = 1.83(1-\alpha) - 0.129. \tag{87}$$

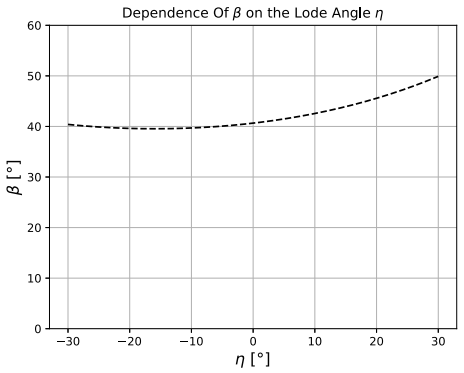

Fig. 6. Possible values for the angle β for the Drucker–Prager-Cap-Model for all possible values of the Lode angle $\eta \in [-30°, 30°]$ and the fitted value of $\theta = 29.72°$.

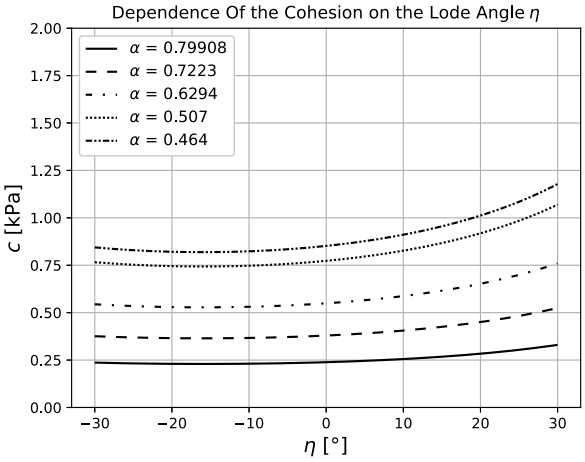

Fig. 7. Possible ranges of the cohesion c at the five measured hardening parameters, depending on the Lode angle η.

2.5.4. Hardening

The isotropic hardening model of the cap-yield surface was parameterized using the preconsolidation pressure measurements, i.e. by measuring the density of the powder after applying the consolidation pressure σ_1. Applying the confined uniaxial compression with σ_1 results in a hydrostatic pressure

$$p_h = \frac{1+\nu_S}{3(1-\nu_S)}\sigma_1 \approx 0.586207\sigma_1, \tag{88}$$

where the Poisson ratio of $\nu_S = 0.275$ for the elastic deformation of the powder was assumed. The fitted value for p_h is then used to parameterize the model for p_c in (78).

To this end, the intersection of the point (p, q) with the yield surface was computed, assuming that for confined uniaxial compression $q = \frac{3(1+\nu_S)}{6(1-\nu_S)}p_h = \gamma p_h$. Solving

$$\Phi_C(p_h, q = \gamma p_h; p_a, R_p, \tan(\beta), c(\alpha)) = 0 \tag{89}$$

results in a quadratic equation for p_a, which has the solution given in Eq. (91). For a graphic illustration, see Fig. 8. Using (69) gets (Eq. (91) is given in Box I):

$$p_c = p_a(1 + R_P\tan(\beta)) - R_P c(\alpha). \tag{90}$$

To parameterize the hardening model, the uniaxial compression, $\alpha = J^P$, was fitted to the increasing pressure p_c. As shown in Fig. 9, five measurements were taken with increasing consolidation pressure. The best fit for the model parameters in Eq. (78) then results in the parametrization of the two constants $K_P = 0.745$ and $\alpha_{min} = 0.538$. For

$$p_a = \frac{p + cR_p^2 \tan(\beta) + \sqrt{p^2 R_p^2 \tan(\beta)^2 + 2pcR_p^2 \tan(\beta) + q^2(R_p^4 \tan(\beta)^2 - R_p^2) + c^2 R_p^2}}{1 - R_p^2 \tan(\beta)^2} \tag{91}$$

Box I.

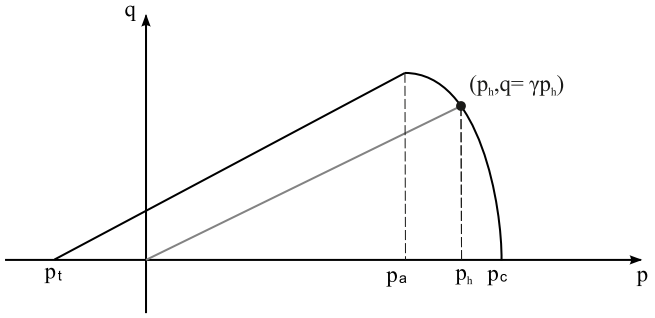

Fig. 8. Solving for the critical yield pressure: for increasing uniaxial load (grey) the stress state (p, q) with $p = \gamma q$ intersects the yield surface $\Phi_C(p, q; p_a, \alpha) = 0$ at $(p_h, \gamma p_h)$. The solution for p_a is given by Eq. (91).

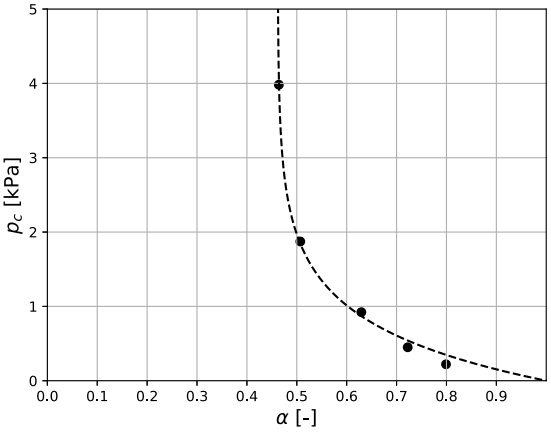

Fig. 9. Fitting of the critical yield pressure to the hardening parameter. Dots indicate data points from flow tester experiments while the dashed line indicates the fitted logarithmic model in Eq. (92).

R_P, a value of $R_P = 0.5$ is postulated. Hence,

$$p_c = -0.745 \log\left(1 - \frac{1-\alpha}{0.538}\right). \tag{92}$$

Yield surfaces. The complete yield surfaces are shown in Fig. 10, for increasing hardening parameter α, parameterized by an increasing cohesion in the Drucker–Prager-Part of the surface, as well as an increasing in the critical yield pressure leading to a moving Cap-Part of the surface towards higher pressures. Also shown are the data points taken with the flow tester, which show a good fit to the data, despite slight deviations from the model.

Verification. The plastic model was verified by simulating a confined uniaxial compression and comparing the result with the data points measured by the flow tester. The resulting curve is shown in Figure S4 in the supplementary material. Overall the model reproduces the measured data well, however there are small differences for low compression ratios. This is most likely due to the approximation of the hydrostatic pressure in the fitting in Eq. (91), which dues not take into account the movement of the intercept during compression. However, since large uniaxial compression is the dominant mode of deformation, we expect the model to produce realistic results.

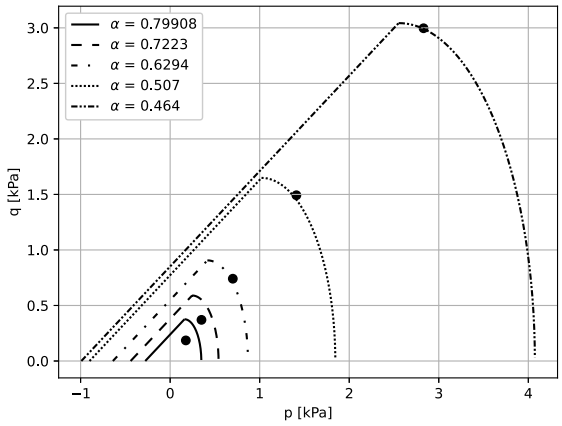

Fig. 10. Parameterized yield surfaces for the Drucker–Prager-Cap-Model, corresponding to the five data points (•) from flow tester experiments with different critical yield pressures.

Table 1
List of physical parameters used.

Property	Parameter	Value
Therm. conductivity	λ_{eff}	0.4 W/m K
Spec. heat cap. $Ca(OH)_2$	$C_{\text{P,Ca(OH)}_2}$	1530 J/kg K
Density $Ca(OH)_2$	$\rho_{\text{Ca(OH)}_2}$	2200 kg/m³
Molar mass $Ca(OH)_2$	$M_{\text{Ca(OH)}_2}$	74 kg/mol
Molar volume $Ca(OH)_2$	$V^m_{\text{Ca(OH)}_2}$	$3.36 \cdot 10^{-5}$ m³/mol
Spec. heat cap. CaO	$C_{\text{P,CaO}}$	934 J/kg K
Density CaO	ρ_{CaO}	3340 kg/m³
Molar mass CaO	M_{CaO}	56 kg/mol
Molar volume CaO	V^m_{CaO}	$1.67 \cdot 10^{-5}$ m³/mol
Water vapor diffusivity	D_{eff}	$9.56 \cdot 10^{-5}$ kg/m³
Rate Const. Hydr.	k_h	0.2 1/s
Rate Const. Dehydr.	k_d	0.05 1/s
Young's modulus solid phase	E_S	5 MPa
Poisson ratio solid phase	ν_S	0.275
Typical particle diameter	d_P	26 µm

2.6. Model solution

The physical model was discretized on a deforming conformal grid over the computational domain $\Omega(t)$, moving with the displacement of the solid phase (the porous powder bed) $\vec{u}_S$, as shown in Fig. 1.

2.6.1. Cylindrical coordinates

To simulate the cylindrical reactor, the model was solved in a quasi-2D setting using cylindrical coordinates (r, ϕ, z). While the reactive transport can be solved in two dimensions, the elasto-plastic model has to account for strains and stresses in the axisymmetric direction. Therefore, it is assumed that there is no induced deformation in the ϕ direction, but the strain in ϵ_ϕ-direction is given by $\epsilon_{\phi\phi} = \frac{u_r}{r}$ and shear strains with an axisymmetric component vanish $\epsilon_{i\phi} = \epsilon_{\phi i} = 0$ for $i \in \{r, z\}$.

2.6.2. Spatial discretization

The reactive transport model described above has been discretized in space using first-order Lagrange finite elements on a conformal grid. The resulting linear system is given for the vector $U = (p, T, x_v, x_s)^T$,

holding the state variables for each node. Furthermore, the kinetic terms of the reactive transport model in Eqs. (31),(38),(35),(20) were discretized in time with the implicit Euler method, resulting in the nonlinear system of equations

$$\mathbf{M}(J^t)\frac{U^{t+1}-U^t}{\delta t} = \mathbf{A}(J^t)U^{t+1} + Q, \tag{93}$$

which must be solved for each time step. It holds the mass matrix

$$\mathbf{M} = \begin{pmatrix} M_{pp} & M_{pT} & M_{px_V} & 0 \\ M_{Tp} & M_{TT} & 0 & M_{Tx_s} \\ 0 & 0 & M_{x_V x_V} & 0 \\ 0 & 0 & 0 & M_{x_S x_S} \end{pmatrix}, \tag{94}$$

the discretized transport operators

$$\mathbf{A} = \begin{pmatrix} A_{pp} & A_{pT} & 0 & 0 \\ A_{Tp} & A_{TT} & 0 & 0 \\ A_{Tx_V} & 0 & A_{x_V x_V} & 0 \\ 0 & 0 & 0 & A_{x_S x_S} \end{pmatrix}, \tag{95}$$

as well as the reaction terms Q.

With the discretized displacement vector given by $V = \vec{u}_S$ and the discretized tensor fields E_P, E_c and F are holding the plastic strain, the chemical strain and the deformation gradient, respectively. The momentum balance Eq. (56) with the linearized strain (59) is then discretized as:

$$0 = \Sigma(V; F, E_p, E_c) + \mathcal{F}(U), \tag{96}$$

with the discrete force vector $\mathcal{F}(U)$. The displacement is discretized with first-order Lagrange finite elements, while the plastic and chemical strains and the displacement gradient are discretized with piecewise constant functions in the finite elements. This results in a consistent discretization as the strains couple to the derivative of the displacement through (59).

2.6.3. Coupling

Both models, for the reactive transport and the mechanics of the powder bed are coupled through the pressure drop inside the powder bed, exerting a force in the bed, as well as the changing porosity of the bed which appears in the transport properties of the powder bed, as well as terms containing $\nabla \cdot \vec{v}_S$, which is approximated, using (5) as:

$$\nabla \cdot \vec{v}_S(t) = \frac{\dot{J}}{J} \approx \frac{J^t - J^{t-1}}{\delta t J^t}. \tag{97}$$

Momentum transfer from the bed to the gas is neglected. As there is no kinetic term in Eq. (45), the coupled system of equations represents Differential–Algebraic-System of equations (DAE).

The reactive transport and mechanical problems were coupled with a Predictor–Corrector (PC) time stepping scheme, as follows:

1. **Reactive Transport Time-Step**
   Solve RT-Model for U^{t+1}:
   $$\mathbf{M}(J^t)\frac{U^{t+1}-U^t}{\delta t} = \mathbf{A}(J^t)U^{t+1} + Q((J^t, \dot{J}^t))$$

2. **Compute trial-stress**
   Solve momentum balance for trial-stress:
   $$\Sigma(V^{tr}; F^t, E_p^t, E_c^{t+1}) + \mathcal{F}(U^{t+1}) = 0$$

3. **Compute plastic-strain increment**
   Solve consistency condition for $\delta\varepsilon_P$:
   $$\Phi(\Sigma(V^{tr} + \rho\mathbb{C} : \delta E_p)) = 0$$
   $$E_p^{t+1} = E_p^t + \delta E_p$$

4. **Compute grid correction**

   4.1. Compute consistent displacement solution V^{t+1}:
   $$0 = \Sigma(V^{t+1}; F^t, E_p^{t+1}, E_c^{t+1}) + \mathcal{F}(U^{t+1})$$

   4.2. Update grid
   $$\varphi^{t+1}(X) = X + V^{t+1}$$
   $$F^{t+1} = \frac{\partial \varphi^{t+1}(X)}{\partial X}$$
   $$J^{t+1} = \det(F)$$
   $$(\nabla \cdot \vec{v}_S)^{t+1} = \frac{J^{t+1} - J^t}{\delta t J^{t+1}}$$

2.6.4. Plastic model

For each timestep, the elasto-plastic model was solved using an explicit return mapping scheme [49,50], where an elastic trial stress is computed, using the previous deformation as well as the current gas pressure and chemical strain

$$\nabla \cdot \sigma^{tr} = \nabla \cdot (\varepsilon - \varepsilon_p^t - \varepsilon_c^{t+1}) = \mathbf{f}^{t+1}. \tag{98}$$

A multi-step method was implemented by iterating over the stresses σ^k. Setting $\sigma^{tr} = \sigma^{k=0}$, the trial stress is used to compute the increment of the plastic multiplier $\delta\lambda_k$, by requiring that the consistency for the active yield surface condition holds, i.e.

$$\Phi\left(\sigma^k + \delta\lambda_i^k\, \mathbb{C} : N_p(\sigma)\right) = 0. \tag{99}$$

Then $\delta\lambda_k$ is approximated by

$$\delta\lambda^k = \kappa \frac{\Phi(\sigma^k; \alpha^k)}{\frac{\partial\Phi(\sigma_k;\alpha^k)}{\partial\sigma} : \mathbb{C} : N_p(\sigma^k)}$$

with the underrelaxation factor $\kappa = 0.66$ and the plastic strain and stress increment is given by

$$\varepsilon_p^{k+1} = \varepsilon_p^k + \delta\lambda^k \sum_i \rho_i \frac{\partial \Psi_i}{\partial \sigma^k},$$
$$\sigma^{k+1} = \sigma^k + \delta\lambda^k \mathbb{C} : N_p(\sigma^k)$$
$$\alpha^{k+1} = \alpha^k + \delta\lambda^k \sum_i \rho_i \frac{\partial \Psi_i(\alpha^k)}{\partial \alpha}$$

If the plastic potential falls below a numerical threshold $\Phi(\sigma^k; \alpha^k) \leq \epsilon_P$, the iteration terminates with

$$\varepsilon_p^{t+1} = \varepsilon_p^{k+1}.$$

2.6.5. Implementation

The numerical model was implemented using Python bindings [51] of the DUNE-FEM module of the DUNE numerics package [52]. The solution of the plastic model in Section 2.6.4 has been implemented in C++ as a CppFunction, which can be called for every finite element from the DUNE-Python interface. All resulting linear systems were solved using the DUNE-ISTL library. The GMRES-Solver was used for the reactive transport and momentum balance equation, with the algebraic multi-grid method used as preconditioner and umfpack as a coarse level solver.

Model validation. The implementation of the reactive transport model presented in the previous sections was validated by computing a 1D test case under the simplified model assumption in [21], assuming a non-deformable powder bed and constant porosity. The authors also modify the density of CaO so that no porosity change occurs during cycling. A comparison of the results (see section S3 in the supplementary material) shows only negligible differences. Since [21] states that the model has been validated with experimental data from [16], this by extension validates our model.

3. Results

To demonstrate the added capabilities of the new model, a test case of a cylindrical fixed bed reactor was simulated, for a duration of five cycles, the first of which is discussed in detail. Then the results over the five cycle simulation are compared with experimental results in [12]. Finally, a brief comparison is presented comparing the new model with existing models from literature.

3.1. Reactor setup

As a test case, we consider a cylindrical fixed bed reactor where only the powder bed is taken as the computational domain (see Fig. 1 for an illustration). Furthermore, we exploit the cylindrical symmetry of the problem and formulate the model in cylindrical coordinates. This allows us to further reduce the computational cost by assuming that $r = 0$ corresponds to the centerline of the reactor. The reactor vessel has a radius of $r = 2.5$ cm and the powder bed has an initial height of $h = 15$ cm. The reactor is closed at the bottom with a sieve that allows gas flow but is blocking the powder. A constant pressure drop is applied to the fixed bed from the inlet at the top to the outlet at the bottom. The numerical values in Table 1 were used for the thermophysical properties of the materials in the powder bed.

Computational grid. The computational domain was discretized on a deforming quadrilinear mesh with 16 cells in the radial direction and 120 cells in the axial direction, as depicted in Figure S1 in the supplementary material. The displacement function was discretized with first order finite elements on the undeformed grid. To determine the error of the spatial discretization, a grid study was conducted by refining and coarsening the grid by by-sections in each direction, and then simulating one full cycle. The results are shown in Figures S2 in the supplementary material and show no significant difference between different resolutions.

The time stepping was varied during the different phases of the cycle. A small times step of $\delta t = 0.06s$ was selected during pressurization, as the powder bed undergoes rapid deformation and a smaller time step would lead to an notable artificial viscosity in the coupling between the reactive transport and the mechanical model. During charging and discharging, a time step of $\delta t = 3s$ seconds was set for a sufficient resolution.

An analogous grid study was conducted for the timestep, with the timestep being varied by factors of two and one complete cycle simulated, for each value. Again, the results are shown in Figures S3(a), S3(b) and S3(c). During the pressurization phase minor discrepancies can be observed in S3(a) in the height of the powder bed for a longer timestep than used in the study, likely due to an artificial viscosity cause by the coupling scheme. However, the results for the charging and discharging are virtually identical for all timesteps. Thus, the chosen discretization was deemed acceptable.

Initial state of the powder bed. It is assumed that the powder is already preconsolidated during the filling process, i.e. the plastic hardening parameter is set to $\alpha(t = 0) = J^{pre} = 0.65$. This results in an initial porosity of $\phi_G(t = 0, J = J^{pre}) = 0.7315$, which is in agreement with experimental evidence and also limits further compression to $\approx 25\%$, which is also a value typically observed in experiments.

Porosity permeability relation. Since the permeability is computed locally from the compression and the SOC, it is not an independent parameter and must be modeled consistently with the porosity. Therefore, the permeability was modeled, such that the bulk, at maximum compaction, i.e. minimum porosity of $\phi_{min} = \phi_G(J^{min}) \approx 61\%$ has a permeability of $k_{bed}(\phi_{min}) \approx 5 \cdot 10^{-12}$ m^2, which is consistent with the literature (see e.g. [20]). This corresponds to setting the effective particle diameter in Eq. (33) to $d_p = 26$ µm.

Table 2
Initial and boundary conditions.

Case	Pres.	Charge	Discharge
Inlet $\partial\Omega_{In}$			
P_{in} [bar]	1.25	1.25	2.25
T_{in} [°C]	600	600	300
$x_{v,in}$ [–]	0.01	0.01	0.46
Outlet $\partial\Omega_{Out}$			
P_{out} [bar]	1	1	2
Lateral $\partial\Omega_{Lat}$			
T_{lat} [°C]	600	600	300
Initial			
P_0 [bar]	1	–	–
T_0 [°C]	400	–	–
$x_{v,0}$ [–]	0.01	–	–
$x_{s,0}$ [–]	0.01	–	–
J^{pre} [–]	0.65	–	–
ϕ_0 [–]	0.73	–	–

Cycling. Five complete cycles were simulated to investigate the irreversible mechanical effects, i.e. powder bed compaction, during cycling. Each cycle consists of 5 stages, where the corresponding BC in Table 2 are applied:

1. **Pressurization:** Buildup of the mass flow and therefore the pressure drop inside the reactor, compacting the powder bed.
2. **Charge (Dehydration):** Dehydration of a $Ca(OH)_2$ powder bed leading to shrinkage of the bed.
3. **Uppressurization:** Ramping the pressure and the temperature BC to the Discharge case over 30 s.
4. **Discharge (Hydration):** Hydration of a CaO powder bed, expanding the bed.
5. **Downpressurization:** Ramping the pressure and the temperature BC to the Discharge case over 30 s.

During the up- and downpressure stages, the reactive transport boundary conditions are ramped linearly between the charge and discharge cases over 30 s. Consequently, no additional BC are given in Table 2. These intermediate stages are necessary because a jump in the boundary conditions caused an instability in the simulation.

Boundary and initial conditions. For the corresponding boundary and initial conditions for the reactive transport and for each stage in the cycling see Table 2. For the symmetry boundary $\partial\Omega_{sym}$ we apply Neuman BC with value 0 for all fields. For the mechanical model it is assumed that the bed is fixed at the outlet $\mathbf{u} = \mathbf{0}$ and stress free $\sigma \cdot n = 0$ at the inlet. On the lateral and symmetry boundaries, mixed boundary conditions are assumed, fixing the bed in the direction perpendicular to the wall, i.e. $\mathbf{u} \cdot n = 0$.

3.2. Simulation results

3.2.1. Pressurization

To simulate the pressurization of the reactor, the corresponding boundary conditions in Table 2 were applied. However, in order to simulate a gradual pressurization over a simulation time of $t^P = 120$ s, the pressure drop was ramped up linearly from zero to the final pressure drop over a period of 30 s from the start. During this period, the pressure of the gas flow on the powder bed steadily increases and compacts the powder bed. Figs. 12 and 13 illustrate the evolution of the porosity and compaction factor J, respectively, from the initial state to the final state.

As shown, compaction begins at the bottom of the vessel and then propagates towards the inlet. After pressurization, the compression is almost homogeneous throughout the bulk of the powder bed, with the

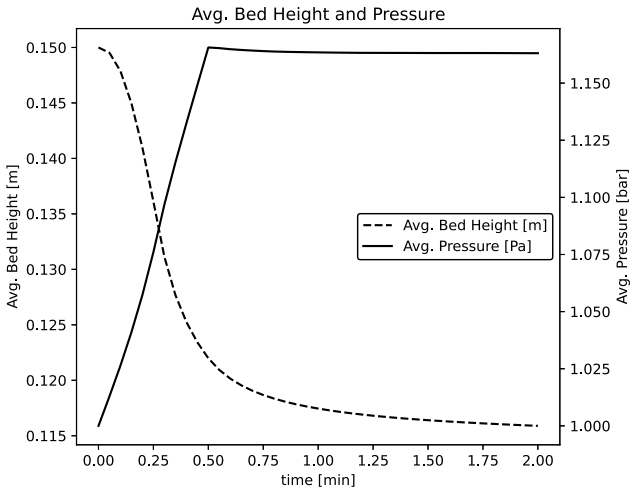

Fig. 11. Average pressure inside the reactor versus the height of the powder bed.

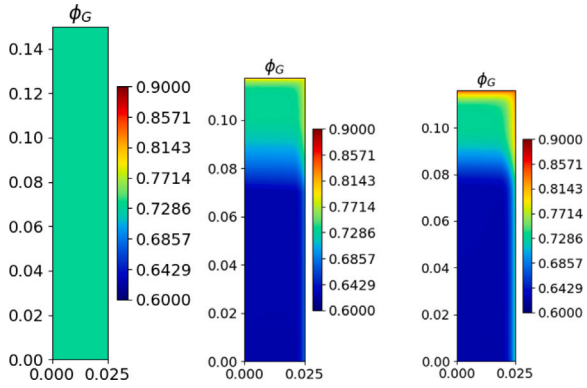

Fig. 12. Porosity of the powder bed during pressurization after: 6 s (left), 30 s (mid) and 60 s (right).

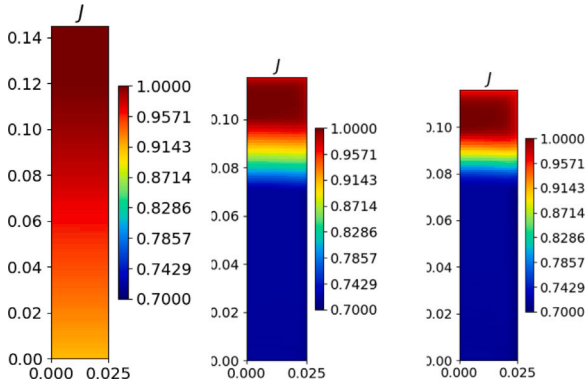

Fig. 13. Compaction factor J of the powder bed during initial pressurization after: 10 s (left), 30 s (mid) and 60 s (right).

exception of a boundary layer at the top facing the gas flow inlet, as shown in the final state plots (right). This follows directly from the porosity dependence of the critical yield pressure shown in Fig. 9 and cannot be reproduced with an elastic constitutive law for the powder bed. In addition, the porosity at the boundary between the inlet and the reactor wall decreases as the dehydration reaction is setting in. The evolution of the bed height with increasing pressure is shown in Fig. 11. As can be observed, the bed compacts by ca. 25% over a period of 2 min, after the final pressure drop is reached.

3.2.2. Charge/discharge-cycle

Taking the pressurized reactor as the initial state (hence no initial conditions in Table 2 for this case), the charging and discharging of the reactor was simulated. The results of the simulation, depicted in Figs. 16 and 18, respectively, for the charging and discharging processes, show the formation of a clearly visible reaction front indicated by the temperature and the SOC plots, which moves from the boundary and inlet towards the interior of the reactor and outlet. One complete cycle was completed in 121 min, and the state of charge, i.e. the molar fraction of CaO, and the average temperature are shown in Fig. 14. As illustrated, a full charge is reached after about 45 min, when the average temperature also reaches its maximum as no heat is consumed by the reaction. After 60 min the BC switch to the uppressurization over 30 s and then the discharge was simulated over 60 min. The uppressurization was omitted in the plot in Fig. 14 to improve readability, resulting in a discontinuity in the temperature. The discharge is completed after 40 min, 5 min earlier than for the charging reaction.

Powder compaction. The plots on the right in Figs. 16 and 18 show the evolution of porosity and compression factor J_P during charging and discharging, respectively. Significant changes occur in the porosity, which varies between 86% and 62%. This effect is due to the difference in the factors ξ_V and ξ_p, which parameterize the microscopic and macroscopic volume changes respectively. As $\xi_V \gg \xi_p$, the majority of the mass loss during dehydration results in an increase in porosity and not in macroscopic shrinkage, and vice versa. The same effect is clearly visible in Fig. 17, showing the simulated height of the bed and its average porosity. During cycling, the average porosity varies strongly between 60% and 80%, while the bed only expands and contracts by less than 10% after compacting by 25% in the initial pressurization.

Furthermore, it is clearly visible, that the height of the powder bed does not revert to its original state after pressurization ($t = 2$ min), hence the powder bed compacts during the cycle. The mechanism underlying the compaction is illustrated in Fig. 15. The Jacobian J and the pressure drop dp are plotted along the center line of the reactor in coordinates of the undeformed configuration. After pressurization (black), a loose boundary layer has formed facing the inlet. During the charging phase, the bed shrinks, yet the boundary layer remains intact (shown in red). However, during the discharge stage, the boundary layer compacts further. This is due to the formation of a dense, low-porosity layer during the onset of the hydration reaction in the vicinity of the inlet, which results in a significant pressure drop near the inlet (depicted in green pressure curve), leading to the compaction of the layer (shown in blue). The state of the reactor corresponding to the green line is also shown in Fig. 18. Therefore, the formation of the reaction front near the inlet contributes to the compaction of the powder bed.

3.3. Five cycle simulation

In total, five complete cycles were simulated to investigate the powder bed compaction, during cycling. The state of charge over the five cycles, i.e. the molar fraction of CaO in the bed, is shown in Fig. 19. As shown, after the 60 s pressurization phase, each cycle lasts 120 min, so the whole cycle is completed after 10 h.

The average temperature and pressure inside the reactor are plotted in Fig. 20. The discontinuities in the temperature and pressure curves are the periodic up- and downpressure phases, which have been omitted from the graph to improve readability. In between, during the hydration and rehydration cycles, the temperature shows the typical profile of the first charge/discharge cycle. The pressure responds dynamically to the temperature changes, oscillating around the baseline pressure for the cycle. This indicates that the mechanical change in the powder bed, at least in the present model, does not have a significant effect on the course of the thermochemical reaction inside the reactor. This is likely due to the fact that the thermochemical reaction is limited by the heat transport from the reactor walls to the bed, and in the model the heat conductivity is independent of the compaction of the material, which is however not realistic.

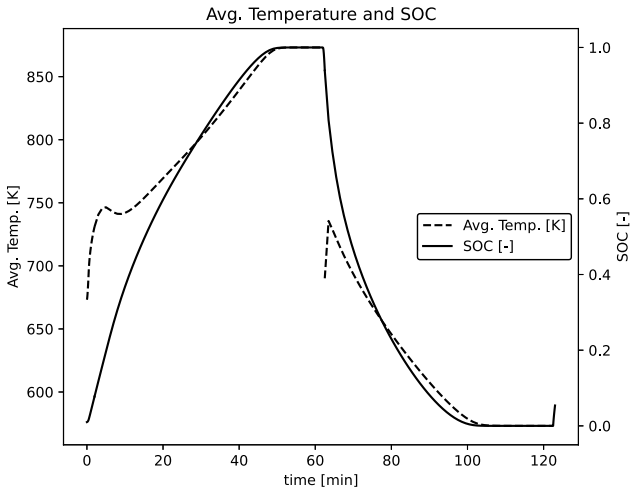

Fig. 14. State of charge and average temperature in the reactor during the first cycle in the simulation.

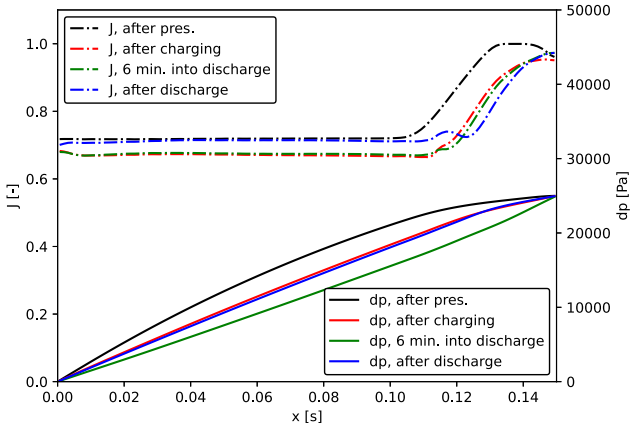

Fig. 15. Jacobian J and pressure drop dp along the center line of the reactor at three point in time: (black) after pressurization, (red) after charging, (green) 6 min. into discharge, (blue) after discharge.

Powder bed compaction. The effect of cycling on the state of the powder bed is shown in Fig. 21. As can be seen, the powder bed compresses rapidly during the initial pressurization phase in the first minute and then contracts and expands periodically. However, unlike the temperature and pressure curves, irreversible effects can be observed during cycling, with a notable compaction during the first cycle and a slight drop in powder bed height between the second and last cycles. This is due to a compaction of the boundary layer at the inlet during hydration. This is further illustrated in Fig. 22, where the thickness of the boundary layer in the porosity near the inlet decreases significantly from the beginning of the first cycle to the end of the 5th cycle. Simulation of these effects is crucial as powder agglomeration is highly dependent on powder consolidation.

3.4. Comparison with experimental data

A quantitative comparison with experiment is beyond the scope of this paper. However, qualitative comparisons can be made with data in Gollsch et al. [12], who conducted experiments with a fixed bed reactor and observed the bed over 10 cycles. Qualitatively, the findings in [12] agree with the predictions from our model. The authors report an initial compaction due to gas flow from 24 cm to 17 cm, or 30% and only a very small decrease in the bed height from 17 cm to 15.75 cm during the subsequent 10 cycles. This was in qualitative agreement with the

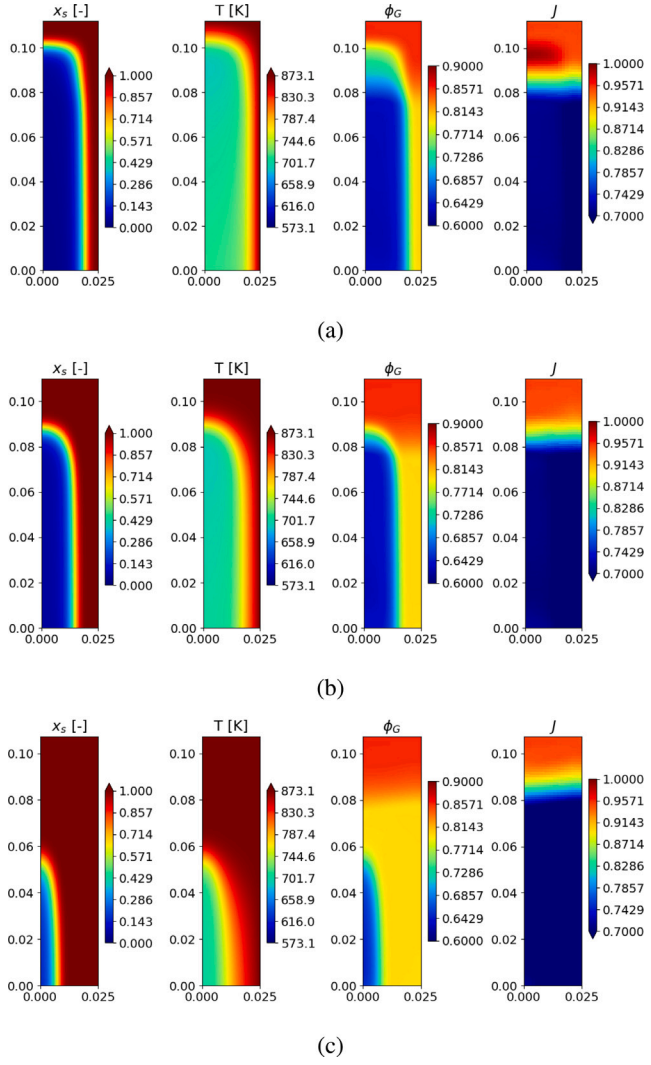

Fig. 16. Simulation of the charging/dehydration of the reactor. From the left to the right: temperature T, local SOC x_s, porosity ϕ_G and expansion factor J. State of the reactor after: (a) 10 min, (b) 20 min, (c) 40 min.

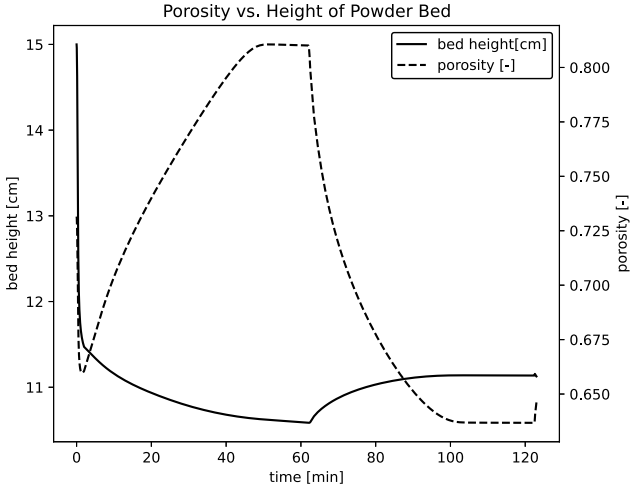

Fig. 17. State of charge and average temperature in the reactor during discharging.

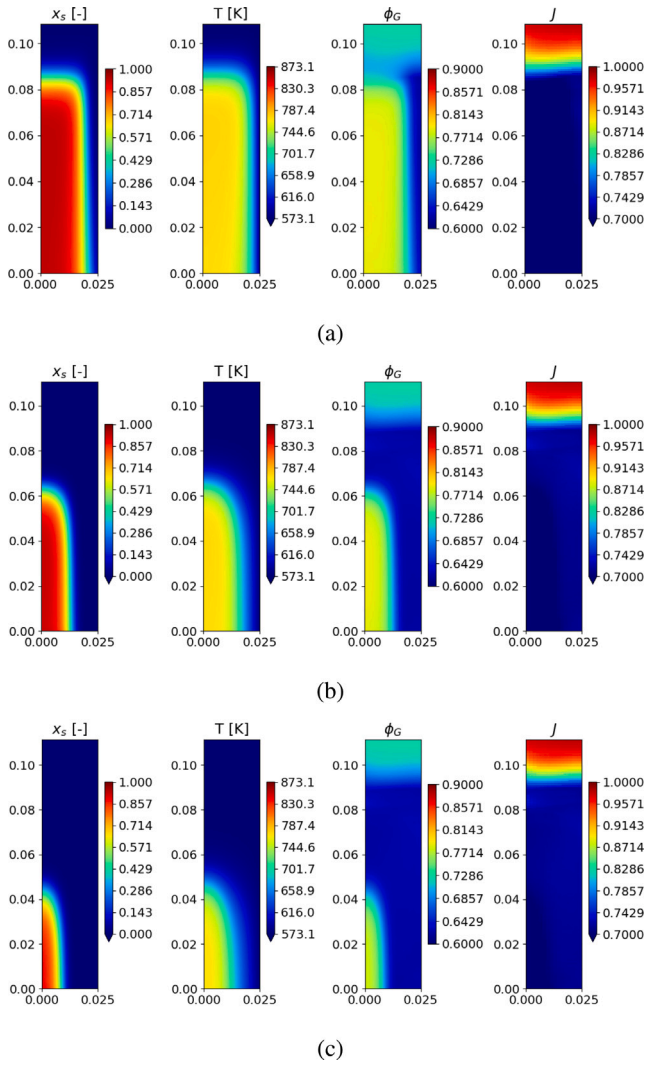

Fig. 18. Simulation of the charging/dehydration of the reactor. From the left to the right: temperature T, local SOC x_s, porosity ϕ_G and expansion factor J. State of the reactor after: (a) 6 min, (b) 20 min, (c) 30 min.

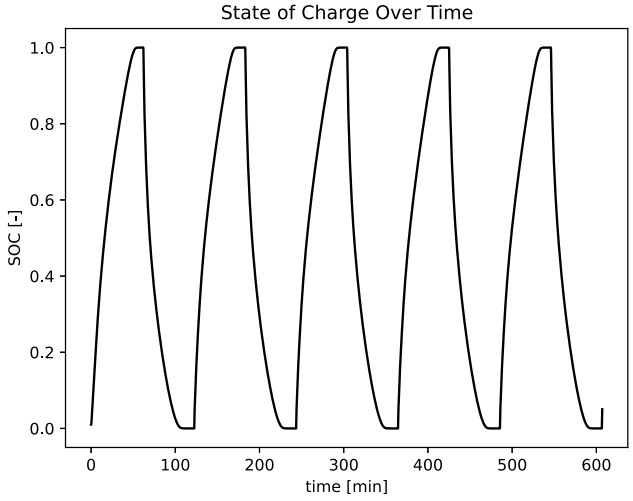

Fig. 19. State of charge during cycling for 5 complete cycles.

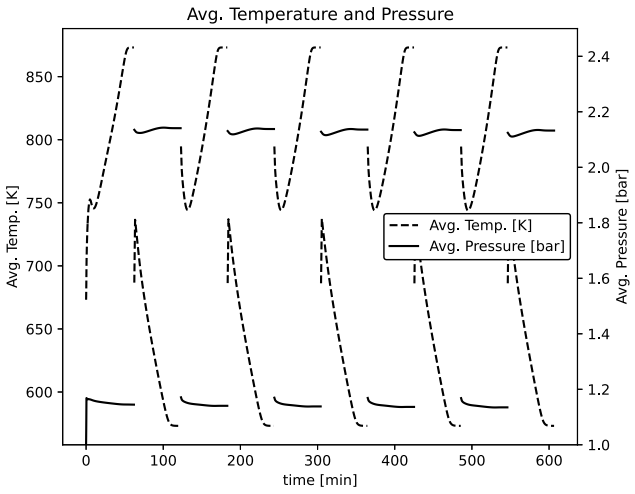

Fig. 20. Average temperature and gas pressure during 5 complete cycles and the initial pressurization in the first minute. Discontinuities in the plots stem from the up- and down-pressure cycles omitted for readability.

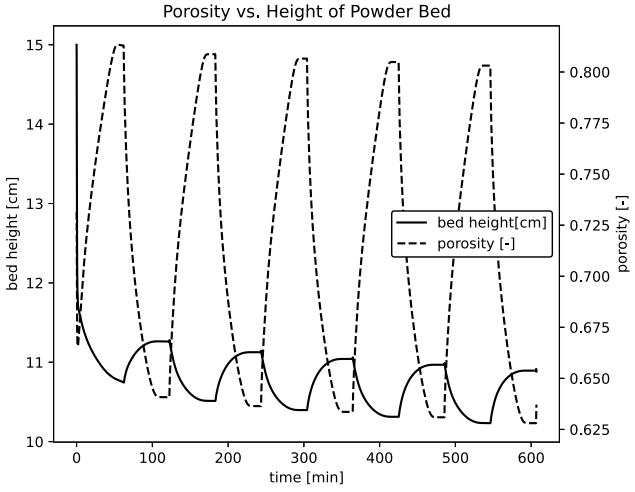

Fig. 21. Porosity and height of the powder bed during 5 complete cycles and the initial pressurization in the first minute.

model simulations over 5 cycles. However, the reported porosities are generally higher than those predicted by our model with 81% porosity before pressurization and 70%–73% for the CaOH phase and 85% for the CaO phase. One possible explanation for this discrepancy could be that the current model does not account for wall friction, which could reduce the compaction of the powder during filling and pressurization. Alternatively, the powder may agglomerate rapidly during the initial cycle, impeding further compaction.

3.5. Model comparison

To quantify the difference between the new model and existing models in the literature, simulations were run with two models which are simplifications of the new model with respect to the porosity-permeability relationship and porosity evolution. The simulated models are:

- Model 1: **Dynamic Powder Bed** full elasto-plastic powder bed
- Model 2: **Static Powder Bed** non-deforming powder bed with constant porosity
- Model 3: **Evolving Porosity** non-deforming powder bed with evolving porosity and corresponding permeability

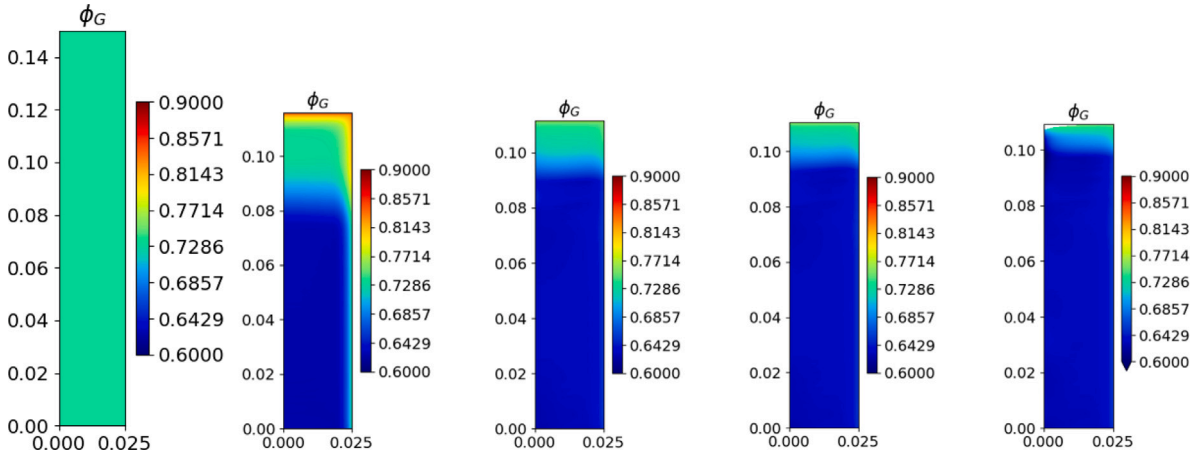

Fig. 22. Compaction of the powder bed during cycling: porosity of the powder bed (from left to right) in the initial state, after pressurization, after one cycle, after two cycles, after five cycles.

The results of the simulations were then compared to investigate the differences between the models. The impact of different modeling assumptions on the cycling is shown in Figs. 23. The first cycle from the previous simulation was chosen for comparison as the state of the bed most closely resembles a fully compacted bed as assumed in the simplified models.

For both Model 2 and Model 3, a maximum compression of $J^{pre} = J^{min} \approx 0.47$ was assumed to approximate a fully compacted state after long cycling. For Model 2, the porosity and permeability are set to the values assumed for the maximally compacted state with, while for Model 3 the porosity is set to $\phi_G = 1 - \phi_S(J^{min})(1 - \xi_V x_S)$, i.e. a static powder bed with a variable porosity depending on the SOC.

As illustrated in Fig. 23(a), the constant porosity model (Model 2) exhibits a slower charge and discharge rate than the models with variable porosity. This is likely due to the slower gas transport. The variable porosity model (Model 3) exhibits a slightly slower reaction rate than the full dynamic bed model. This is likely due to the smaller bed size, resulting from the absence of a low-porosity layer near the inlet, which can be observed in the dynamic model. This in turn impedes gas and heat transport from the inlet to the reaction front. A heat transfer limitation is clearly visible in Fig. 23(b). Overall, the discrepancies between the dynamic model and Model 3 are relatively minor, although this is contingent upon the assumption of a constant thermal conductivity within the bulk and perfect contact with the reactor walls, both of which are known to be significant thermal resistances within the reactor.

3.6. Discussion

We believe that the proposed model provides a framework for the modeling of the dynamics and structural changes in fixed bed TECS reactors. A comparison with experimental findings in [12] indicates that the model derived in this paper, when properly parameterized, can qualitatively reproduce irreversible effects due to powder compaction during cycling. The model can be readily extended to include further effects, such as fracturing of a fully solidified bed. Nevertheless, further research is necessary to model and simulate additional effects, such as the agglomeration of powder particles resulting from the chemical reaction, the fundamental physics of which still needs to be explored. Also, the parametrization of the mechanical model is incomplete due to the ambiguity in the model parameters arising from the unknown lode angle and the influence of wall friction. However, this can easily be remedied by extending the available data to triaxial tests or experiments using die compression as e.g. in Han et al. [41]. The incorporation of wall friction, properly parameterized, could explain differences in the predicted porosity and permeability from the

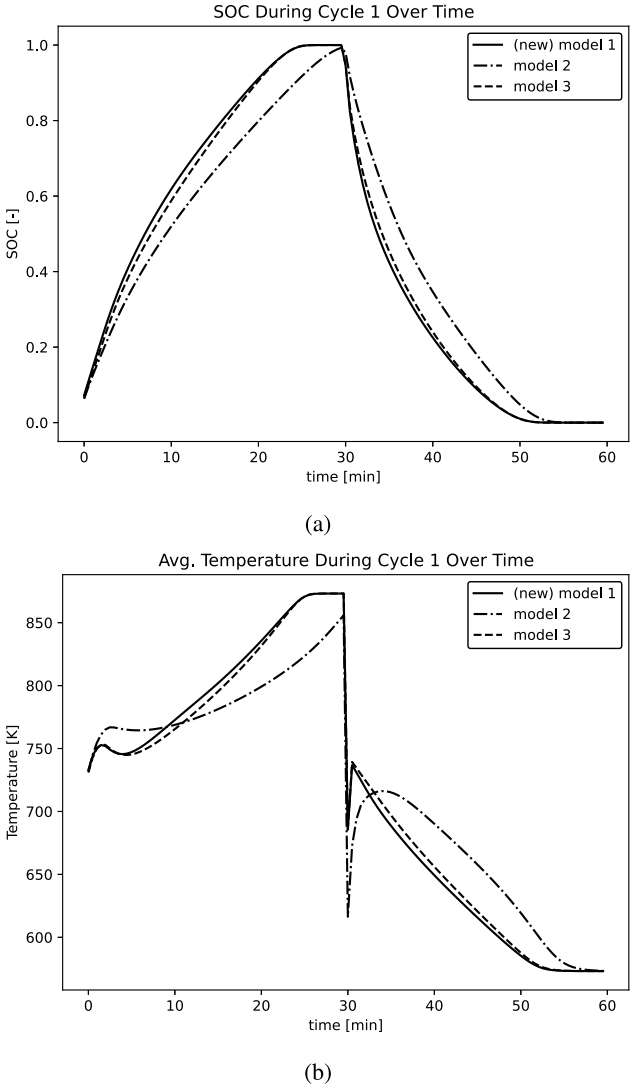

Fig. 23. Comparison between the SOC (top) and average temperature (bottom) between different powder bed models over time during one cycle.

experimentally as reported in [12].

Furthermore, the model can be extended to include a variable thermal conductivity depending on the compaction of the powder bed, which could also depend on the mechanical pressure in the powder, which can only be calculated by a mechanical model of the bed itself. This is particularly true for the pressure exerted by the reactor walls, where wall detachment or contact pressure is known to have a strong limiting effect on heat transfer from the wall to the powder bed (see [7]). Heat conducting structures, such as pipes in [32] or fins [7], are sometimes used to increase the effective surface area of the reactor wall and improve thermal contact. As the thermal resistance depends on the interaction between the reactor geometry and the powder bed deformation, our predictive model could be used to optimize pipe placements or fin geometries in a fixed bed reactor. The pressure boundary conditions also have a strong influence on the powder bed dynamics. Modeling the compaction due to gas pressure could lead to optimized cycling protocols where the gas pressure is regulated over time. In both cases, modeling can be used to achieve a desired degree of compaction, depending on the reactor geometry and application.

3.7. Conclusion

In conclusion, the presented framework represents a significant advancement in the field of TCES modeling, incorporating the dynamics of the powder bed in fixed bed reactors. The model has been developed from porous media theory, that was specialized for TCES applications and includes a large strain elasto-plastic mechanical model of the powder bed. It was further demonstrated that the model can be parameterized using only flow tester experiments. Numerical simulations over multiple cycles have shown that the model can reproduce the compaction of the powder within fixed bed reactors, which was observed in experiments, but which cannot be simulated with static models. This is due to a layer with low porosity which is formed by the expanding powder during the hydration process, close to the inlet. When extended to include additional effects such as powder agglomeration, and parameterized with additional experimental data, the new framework has the potential to significantly enhance the predictive powder of TCES models and can lead to new avenues for the computational design of TCES reactors.

CRediT authorship contribution statement

Torben Prill: Writing – original draft, Visualization, Validation, Software, Methodology, Investigation, Formal analysis, Data curation, Conceptualization. **Arnulf Latz:** Writing – review & editing, Project administration, Funding acquisition, Conceptualization. **Thomas Jahnke:** Writing – review & editing, Supervision, Project administration, Conceptualization.

Declaration of competing interest

The authors declare that they have no known competing financial interests or personal relationships that could have appeared to influence the work reported in this paper.

Appendix A. Supplementary data

Supplementary material related to this article can be found online at https://doi.org/10.1016/j.apenergy.2025.125275.

Data availability

Data will be made available on request.

References

[1] Criado YA, Huille A, Rougé S, Abanades JC. Experimental investigation and model validation of a cao/ca(oh)2 fluidized bed reactor for thermochemical energy storage applications. Chem Eng J 2017;313:1194–205. http://dx.doi.org/10.1016/j.cej.2016.11.010, URL https://www.sciencedirect.com/science/article/pii/S1385894716315716.

[2] Schaube F, Wörner A, Tamme R. High temperature thermochemical heat storage for concentrated solar power using gas–solid reactions. J Solar Energy Eng 2011;133(3). http://dx.doi.org/10.1115/1.4004245.

[3] Papapetrou M, Kosmadakis G, Cipollina A, La Commare U, Micale G. Industrial waste heat: Estimation of the technically available resource in the eu per industrial sector, temperature level and country. Appl Therm Eng 2018;138:207–16. http://dx.doi.org/10.1016/j.applthermaleng.2018.04.043.

[4] Wang K, Yan T, Li RK, Pan WG. A review for ca(oh)2/cao thermochemical energy storage systems. J Energy Storage 2022;50. http://dx.doi.org/10.1016/j.est.2022.104612.

[5] Kuipers JAM, Prins W, Van Swaaij WPM. Numerical calculation of wall-to-bed heat-transfer coefficients in gas-fluidized beds. AIChE J 2004;38(7):1079–91. http://dx.doi.org/10.1002/aic.690380711.

[6] Schaube F, Utz I, Wörner A, Müller-Steinhagen H. De- and rehydration of ca(oh)2 in a reactor with direct heat transfer for thermo-chemical heat storage. part b: Validation of model. Chem Eng Res Des 2013;91(5):865–73. http://dx.doi.org/10.1016/j.cherd.2013.02.019.

[7] Stengler J, Bürger I, Linder M. Performance analysis of a gas-solid thermochemical energy storage using numerical and experimental methods. Int J Heat Mass Transfer 2021;167:120797. http://dx.doi.org/10.1016/j.ijheatmasstransfer.2020.120797, URL https://www.sciencedirect.com/science/article/pii/S0017931020337352.

[8] Dai L, Long X-F, Lou B, Wu J. Thermal cycling stability of thermochemical energy storage system ca(oh)2/cao. Appl Therm Eng 2018;133:261–8. http://dx.doi.org/10.1016/j.applthermaleng.2018.01.059.

[9] Risthaus K, Bürger I, Lutz M, Funayama S, Kato Y, Linder M, Schmidt M. Experimental and numerical investigation of the dehydration of ca(oh)2 at low steam pressures. Processes 2022;10:325. http://dx.doi.org/10.3390/pr10020325.

[10] Xu M, Huai X, Cai J. Agglomeration behavior of calcium hydroxide/calcium oxide as thermochemical heat storage material: A reactive molecular dynamics study. J Phys Chem C 2017;121(5):3025–33. http://dx.doi.org/10.1021/acs.jpcc.6b08615.

[11] Afflerbach S, Trettin R. A fundamental study on the mechanistic impact of repeated de- and rehydration of ca(oh)2 on thermochemical cycling in technical scale. Adv Mater Lett 2019;10:312–8. http://dx.doi.org/10.5185/amlett.2019.2190.

[12] Gollsch M, Linder M. Influence of structural changes on gas transport properties of a cycled cao/ca(oh)2 powder bulk for thermochemical energy storage. J Energy Storage 2023;73:108790. http://dx.doi.org/10.1016/j.est.2023.108790, URL https://www.sciencedirect.com/science/article/pii/S2352152X23021874.

[13] Nagel T, Beckert S, Lehmann C, Glaser R, Kolditz O. Multi-physical continuum models of thermochemical heat storage and transformation in porous media and powder beds-a review. Appl Energy 2016;178:323–45. http://dx.doi.org/10.1016/j.apenergy.2016.06.051, URL <GotoISI>://WOS:000382340700026.

[14] MacielCamacho A, Hernandez HR, Hills AWD, Morales RD. Hydration kinetics of lime. Isij Int 1997;37(5):468–76. http://dx.doi.org/10.2355/isijinternational.37.468, URL <GotoISI>://WOS:A1997XB16200006.

[15] Fujii I, Ishino M, Akiyama S, Murthy MS, Rajanandam KS. Behavior of ca(oh)2/cao pellet under dehydration and hydration. Sol Energy 1994;53(4):329–41. http://dx.doi.org/10.1016/0038-092x(94)90036-1, URL <GotoISI>://WOS:A1994PK84600004.

[16] Schaube F, Koch L, Wörner A, Müller-Steinhagen H. A thermodynamic and kinetic study of the de- and rehydration of ca(oh)2 at high h2o partial pressures for thermo-chemical heat storage. Thermochim Acta 2012;538:9–20. http://dx.doi.org/10.1016/j.tca.2012.03.003.

[17] Favergeon L, Pijolat M, Soustelle M. Surface nucleation and anisotropic growth models for solid-state reactions. Thermochim Acta 2017;654:18–27. http://dx.doi.org/10.1016/j.tca.2017.05.004.

[18] Koga N, Favergeon L, Kodani S. Impact of atmospheric water vapor on the thermal decomposition of calcium hydroxide: a universal kinetic approach to a physico-geometrical consecutive reaction in solid-gas systems under different partial pressures of product gas. Phys Chem Chem Phys 2019;21(22):11615–32. http://dx.doi.org/10.1039/c9cp01327j, URL https://www.ncbi.nlm.nih.gov/pubmed/31114819.

[19] Manzano H, Pellenq RJ, Ulm FJ, Buehler MJ, van Duin AC. Hydration of calcium oxide surface predicted by reactive force field molecular dynamics. Langmuir 2012;28(9):4187–97. http://dx.doi.org/10.1021/la204338m, URL https://www.ncbi.nlm.nih.gov/pubmed/22316164.

[20] Nagel T, Shao H, Singh AK, Watanabe N, Roßkopf C, Linder M, Wörner A, Kolditz O. Non-equilibrium thermochemical heat storage in porous media: Part 1 – conceptual model. Energy 2013;60:254–70. http://dx.doi.org/10.1016/j.energy.2013.06.025.

[21] Shao H, Nagel T, Roßkopf C, Linder M, Wörner A, Kolditz O. Non-equilibrium thermo-chemical heat storage in porous media: Part 2 – a 1d computational model for a calcium hydroxide reaction system. Energy 2013;60. http://dx.doi.org/10.1016/j.energy.2013.07.063, URL https://www.ncbi.nlm.nih.gov/pubmed/22316164.

[22] Nagel T, Shao H, Roßkopf C, Linder M, Wörner A, Kolditz O. The influence of gas–solid reaction kinetics in models of thermochemical heat storage under monotonic and cyclic loading. Appl Energy 2014;136:289–302. http://dx.doi.org/10.1016/j.apenergy.2014.08.104.

[23] Wang W, Kolditz O, Nagel T. Parallel finite element modelling of multi-physical processes in thermochemical energy storage devices. Appl Energy 2017;185:1954–64. http://dx.doi.org/10.1016/j.apenergy.2016.03.053, URL https://www.sciencedirect.com/science/article/pii/S0306261916303737, clean, Efficient and Affordable Energy for a Sustainable Future.

[24] Schaube F, Kohzer A, Schutz J, Worner A, Muller-Steinhagen H. De- and rehydration of ca(oh)(2) in a reactor with direct heat transfer for thermo-chemical heat storage. part a: Experimental results. Chem Eng Res Des 2013;91(5):856–64. http://dx.doi.org/10.1016/j.cherd.2012.09.020, URL <GotoISI>://WOS:000319786200010.

[25] Schaube F, Utz I, Worner A, Muller-Steinhagen H. De- and rehydration of ca(oh)(2) in a reactor with direct heat transfer for thermo-chemical heat storage. part b: Validation of model. Chem Eng Res Des 2013;91(5):865–73. http://dx.doi.org/10.1016/j.cherd.2013.02.019, URL <GotoISI>://WOS:000319786200011.

[26] Wang M, Chen L, He P, Tao W-Q. Numerical study and enhancement of ca(oh)2/cao dehydration process with porous channels embedded in reactors. Energy 2019;181:417–28. http://dx.doi.org/10.1016/j.energy.2019.05.184.

[27] Risthaus K, Bürger I, Linder M, Schmidt M. Numerical analysis of the hydration of calcium oxide in a fixed bed reactor based on lab-scale experiments. Appl Energy 2020;261:114351. http://dx.doi.org/10.1016/j.apenergy.2019.114351, URL https://www.sciencedirect.com/science/article/pii/S0306261919320380.

[28] Ranjha Q, Oztekin A. Numerical analyses of three-dimensional fixed reaction bed for thermochemical energy storage. Renew Energy 2017;111:825–35. http://dx.doi.org/10.1016/j.renene.2017.04.062.

[29] Ye H, Tao YB, Wu ZH. Performance improvement of packed bed thermochemical heat storage by enhancing heat transfer and vapor transmission. Appl Energy 2022;326. http://dx.doi.org/10.1016/j.apenergy.2022.119946.

[30] Han XC, Xu HJ, Zhao CY. Design and performance evaluation of multi-layered reactor for calcium-based thermochemical heat storage with multi-physics coupling. Renew Energy 2022;195:1324–40. http://dx.doi.org/10.1016/j.renene.2022.06.120.

[31] Wang W, Shuai Y, Yang J, Lougou BG, Huang Y. Heat transfer and heat storage characteristics of calcium hydroxide/oxide based on shell-tube thermochemical energy storage device. Renew Energy 2023;218:119364. http://dx.doi.org/10.1016/j.renene.2023.119364, URL https://www.sciencedirect.com/science/article/pii/S096014812301279X.

[32] Wang M, Chen L, Zhou Y, Tao W-Q. Numerical simulation of the calcium hydroxide/calcium oxide system dehydration reaction in a shell-tube reactor. Appl Energy 2022;312. http://dx.doi.org/10.1016/j.apenergy.2022.118778.

[33] Michel B, Mazet N, Mauran S, Stitou D, Xu J. Thermochemical process for seasonal storage of solar energy: Characterization and modeling of a high density reactive bed. Energy 2012;47(1):553–63. http://dx.doi.org/10.1016/j.energy.2012.09.029.

[34] Seitz G, Helmig R, Class H. A numerical modeling study on the influence of porosity changes during thermochemical heat storage. Appl Energy 2020;259. http://dx.doi.org/10.1016/j.apenergy.2019.114152.

[35] Xu Q, Sun J, Ma Z, Xie R, Wei J. Influences of variable porosity on cao/ca(oh)2 thermochemical energy storage characteristics in direct/indirect heated reactor. Appl Therm Eng 2022;208. http://dx.doi.org/10.1016/j.applthermaleng.2022.118231.

[36] Stephan P, Kabelac S, Kind M, Mewes D, Schaber K, Wetzel T, editors. VDI-wärmeatlas. Berlin, Heidelberg: Springer Vieweg; 2019, http://dx.doi.org/10.1007/978-3-662-52989-8.

[37] Miehe C, Apel N, Lambrecht M. Anisotropic additive plasticity in the logarithmic strain space: modular kinematic formulation and implementation based on incremental minimization principles for standard materials. Comput Methods Appl Mech Engrg 2002;191(47):5383–425. http://dx.doi.org/10.1016/S0045-7825(02)00438-3, URL https://www.sciencedirect.com/science/article/pii/S0045782502004383.

[38] MacMinn CW, Dufresne ER, Wettlaufer JS. Large deformations of a soft porous material. Phys Rev Appl 2016;5:044020. http://dx.doi.org/10.1103/PhysRevApplied.5.044020.

[39] Michrafy A, Ringenbacher D, Tchoreloff P. Modelling the compaction behaviour of powders: Application to pharmaceutical powders. Powder Technol 2002;127:257–66. http://dx.doi.org/10.1016/S0032-5910(02)00119-5.

[40] Garner S, Strong J, Zavaliangos A. The extrapolation of the Drucker–Prager/cap material parameters to low and high relative densities. Powder Technol 2015;283:210–26. http://dx.doi.org/10.1016/j.powtec.2015.05.027.

[41] Han L, Elliott J, Bentham A, Mills A, Amidon G, Hancock B. A modified Drucker–Prager cap model for die compaction simulation of pharmaceutical powders. Int J Solids Struct 2008;45(10):3088–106. http://dx.doi.org/10.1016/j.ijsolstr.2008.01.024.

[42] Wu C-Y, Ruddy O, Bentham A, Hancock B, Best S, Elliott J. Modelling the mechanical behaviour of pharmaceutical powders during compaction. Powder Technol 2005;152:107–17. http://dx.doi.org/10.1016/j.powtec.2005.01.010.

[43] Drucker DC, Gibson RE, Henkel DJ. Soil mechanics and work-hardening theories of plasticity. Trans Am Soc Civ Eng 1957;122(1):338–46. http://dx.doi.org/10.1061/TACEAT.0007430.

[44] de Souza Neto EA, Perić D, Owen DRJ. Finite strain elastoplasticity. vol. 14, John Wiley & Sons, Ltd; 2008, p. 573–645. http://dx.doi.org/10.1002/9780470694626.ch14.

[45] Cuitiño A, Ortiz M. A material independent method for extending stress update algorithms to finite plasticity with multiplicative kinematics. Eng Comput 1992;9:437–51. http://dx.doi.org/10.1108/eb023876.

[46] Dolarevic S, Ibrahimbegovic A. A modified three-surface elasto-plastic cap model and its numerical implementation. Comput Struct 2007;85(7):419–30. http://dx.doi.org/10.1016/j.compstruc.2006.10.001.

[47] Büttner J, Simeon B. Runge–Kutta methods in elastoplasticity. Appl Numer Math 2002;41(4):443–58.

[48] Gollsch M, Afflerbach S, Angadi B, Linder M. Investigation of calcium hydroxide powder for thermochemical storage modified with nanostructured flow agents. Sol Energy 2020;201:810–8. http://dx.doi.org/10.1016/j.solener.2020.03.033.

[49] Simo JC, Hughes TJ. Computational inelasticity. vol. 7, Springer Science & Business Media; 2006.

[50] Krieg RD, Krieg D. Accuracies of numerical solution methods for the elastic-perfectly plastic model. J Press Vessel Technol-Trans Asme 1977;99:510–5.

[51] Dedner A, Nolte M. The dune python module. 2018, ArXiv URL https://ui.adsabs.harvard.edu/abs/2018arXiv180705252D arXiv:1807.05252.

[52] Bastian P, Blatt M, Dedner A, Dreier N-A, Engwer C, Fritze R, Gräser C, Grüninger C, Kempf D, Klöfkorn R, Ohlberger M, Sander O. The dune framework: Basic concepts and recent developments. Comput Math Appl 2021;81:75–112. http://dx.doi.org/10.1016/j.camwa.2020.06.007.